

## THE KILOPARSEC-SCALE KINEMATICS OF HIGH-REDSHIFT STAR-FORMING GALAXIES

DAVID R. LAW<sup>1,6</sup>, CHARLES C. STEIDEL<sup>2</sup>, DAWN K. ERB<sup>3</sup>, JAMES E. LARKIN<sup>1</sup>, MAX PETTINI<sup>4</sup>, ALICE E. SHAPLEY<sup>1</sup>, AND  
SHELLEY A. WRIGHT<sup>5</sup>

<sup>1</sup> Department of Physics and Astronomy, University of California, Los Angeles, CA 90095, USA; [drlaw@astro.ucla.edu](mailto:drlaw@astro.ucla.edu), [larkin@astro.ucla.edu](mailto:larkin@astro.ucla.edu), [aes@astro.ucla.edu](mailto:aes@astro.ucla.edu)

<sup>2</sup> Department of Astronomy, California Institute of Technology, MS 105-24, Pasadena, CA 91125, USA; [ccs@astro.caltech.edu](mailto:ccs@astro.caltech.edu)

<sup>3</sup> Department of Physics, University of California, Santa Barbara, CA 93106, USA; [dawn@physics.ucsb.edu](mailto:dawn@physics.ucsb.edu)

<sup>4</sup> Institute of Astronomy, Madingley Road, Cambridge CB3 0HA, UK; [pettini@ast.cam.ac.uk](mailto:pettini@ast.cam.ac.uk)

<sup>5</sup> Center for Cosmology, Department of Physics & Astronomy, University of California, Irvine, CA 92697, USA; [saw@uci.edu](mailto:saw@uci.edu)

Received 2009 January 19; accepted 2009 March 27; published 2009 May 18

### ABSTRACT

We present the results of a spectroscopic survey of the kinematic structure of star-forming galaxies at redshift  $z \sim 2\text{--}3$  using Keck/OSIRIS integral field spectroscopy. Our sample is comprised of 12 galaxies between redshifts  $z \sim 2.0$  and  $2.5$  and one galaxy at  $z \sim 3.3$  which are well detected in either  $H\alpha$  or  $[O\ III]$  emission. These galaxies are generally representative of the mean stellar mass of star-forming galaxies at similar redshifts, although they tend to have star formation rate surface densities slightly higher than the mean. These observations were obtained in conjunction with the Keck laser guide star adaptive optics system, with a typical angular resolution after spatial smoothing  $\sim 0''.15$  (approximately 1 kpc at the redshift of the target sample). At most five of these 13 galaxies have spatially resolved velocity gradients consistent with rotation while the remaining galaxies have relatively featureless or irregular velocity fields. All of our galaxies show local velocity dispersions  $\sim 60\text{--}100\text{ km s}^{-1}$ , suggesting that (particularly for those galaxies with featureless velocity fields) rotation about a preferred axis may not be the dominant mechanism of physical support. While some galaxies show evidence for major mergers such evidence is unrelated to the kinematics of individual components (one of our strongest merger candidates also exhibits unambiguous rotational structure), refuting a simple bimodal disk/merger classification scheme. We discuss these data in light of complementary surveys and extant UV-IR spectroscopy and photometry, concluding that the dynamical importance of cold gas may be the primary factor governing the observed kinematics of  $z \sim 2$  galaxies. We conclude by speculating on the importance of mechanisms for accreting low angular momentum gas and the early formation of quasi-spheroidal systems in the young universe.

*Key words:* galaxies: high-redshift – galaxies: kinematics and dynamics – galaxies: starburst

*Online-only material:* color figures

### 1. INTRODUCTION

Galaxies are the discrete luminous building blocks of the visible universe, tracing the development of gravitational structures across cosmic ages. The earliest galaxies likely formed near the density peaks of the primordial power spectrum (e.g., Bardeen et al. 1986) which were able to decouple from the cosmic expansion at early times and form a burst of stars from the primordial gas. As time progressed however, these chaotic proto-galaxies gradually evolved, merging with their neighbors in newly collapsing dark matter halos, accreting greater quantities of gaseous fuel from a filamentary intergalactic medium (IGM), and polluting their environments with the metallic detritus of their early stellar generations. It is at intermediate redshifts  $z \sim 2\text{--}3$  that these morphologically irregular, juvenile galaxies are thought to have formed the majority of the stellar mass which we observe in modern-day galaxies (Dickinson et al. 2003; Reddy et al. 2008). Through a combination of galaxy–galaxy mergers, rapid star formation, and secular evolution, these galaxies experienced a strong morphological transformation into the coherent structures of the Hubble sequence which have predominated since redshift  $z \sim 1$  (Giavalisco et al. 1996; Papovich et al. 2005).

Despite our growing knowledge of the broad global characteristics of high redshift galaxies (e.g., Erb et al. 2006c; Reddy et al. 2006a; Papovich et al. 2006; Cowie & Barger 2008; and

references therein), our understanding of their internal structure and dynamical evolution has been limited by their small angular size, typically  $\lesssim 1$  arcsec. Such objects are generally not well resolved by the ground-based imaging and spectroscopy which form the backbone of our observational data. This limitation precludes us from addressing such questions as: (i) what are the triggering and regulation mechanisms of their starbursts? (ii) Does star formation occur in the (circum)nuclear regions of dynamically relaxed systems or as a result of tidal shocks induced by major mergers? (iii) Do individual star-forming regions follow a global abundance pattern or are there strong variations in chemical enrichment within a galaxy? Each of these distinctions has implications for the evolution and development of structure and stellar populations within a given galaxy.

One of the most promising means to investigate these questions is studying the ionized gas surrounding bright star-forming regions produced by the flood of energetic photons from young stars. Excited atoms in this gas lose energy predominantly by the emission of strong rest-frame optical nebular emission lines (redshifted into the near-infrared (NIR) for galaxies at  $z \sim 2\text{--}3$ ) such as  $H\alpha$ ,  $H\beta$ ,  $[O\ II]$ ,  $[O\ III]$ , and  $[N\ II]$ . The relative strengths of these lines encode information about the chemical composition of the gas and the shape of the ionizing spectrum, permitting deduction of the metallicity and star formation rates (SFRs) of the emission regions. These emission features also have narrow natural line widths and are good kinematic tracers of the ionized gas.

<sup>6</sup> Hubble Fellow.

Such efforts using slit spectroscopy (e.g., Pettini et al. 2001 at  $z \sim 3$ ; Erb et al. 2004, 2006b, 2006c at  $z \sim 2$ ; Weiner et al. 2006 at  $z \sim 1$ ) have suggested that the kinematics of these galaxies may frequently be inconsistent with simple rotationally supported gas disk models. However, these studies have been limited by the small angular size of typical galaxies relative to the atmospheric seeing. Often there may be only 1–2 spatially independent samples across the face of a given galaxy, and additional uncertainty may be introduced by the misalignment of the slit with the (a priori) unknown kinematic axis. It is therefore unclear whether the high observed velocity dispersion is genuine or caused by the smearing of unresolved kinematic structure, such as disklike rotation or merging clumps.

The recent advent of adaptive optics (AO) on 10 m class telescopes has offered the opportunity to overcome the limitations previously imposed by atmospheric turbulence by rapidly correcting the distorted wavefront using deformable mirrors. Paired with integral-field spectroscopy (IFS), it is possible to obtain diagnostic spectra of spatial regions resolved on scales of the order of 100 milliarcseconds (mas), corresponding to roughly 1 kpc at redshift  $z \sim 2$ –3. The data provide an empirical answer to whether the velocity fields of galaxies in the early universe are predominantly represented by virialized disklike systems, major mergers, or some other dynamical structure, and whether the resulting star formation is uniform in its properties across a given galaxy or exhibits regional variation on kiloparsec scales.

Early results from such IFS programs with (Genzel et al. 2006; Law et al. 2007a; Wright et al. 2007, 2009) and without (Förster Schreiber et al. 2006; Bouché et al. 2007; Genzel et al. 2008; Nesvadba et al. 2008; van Starckenburg et al. 2008)<sup>7</sup> AO, in addition to a small number of galaxies observed with the aid of gravitational lensing (Nesvadba et al. 2006; Swinbank et al. 2007; Stark et al. 2008; T. Jones et al. 2009, in preparation), have helped confirm that the high velocity dispersion is an intrinsic property of high-redshift galaxies. The total number of individual galaxies observed however is extremely small, and considerable disagreement remains as to the underlying nature of the dynamical structure of these galaxies, with Genzel et al. (2008, and references therein) suggesting that rotationally supported gaseous disks form the majority of the bright galaxy population while Law et al. (2007a) favor a significantly lower rotation fraction with the majority of galaxies kinematically dominated by their high velocity dispersions.

In this paper, we greatly expand the original sample of Law et al. (2007a) by presenting the spatially resolved laser guide star adaptive optics (LGSAO) spectroscopy of an additional 10 galaxies at redshifts  $2.0 \lesssim z \lesssim 2.5$ . With the larger sample size it is possible to draw broader conclusions about the kinematical characteristics of the galaxy population. The paper is structured as follows. In Section 2, we describe our sample selection, observational technique, and data reduction algorithms. In Section 3, we discuss the physical properties of our galaxies, particularly their morphological (Section 3.1) and kinematic (Section 3.3) structures and stellar populations (Section 3.2). The characteristics of each of our 13 galaxies are discussed individually in detail in Section 4. Section 5 discusses the characteristics of the global population, comparing to recent observations by other groups in Section 5.2 and exploring possible implications for gas accretion and formation mechanisms in Sections 5.3 and 5.4. We conclude with a brief

summary in Section 6, while a derivation of the statistical properties of an ensemble of inclined systems is included in the Appendix. We assume a standard lambda cold dark matter ( $\Lambda$ CDM) cosmology based on three-year *WMAP* data (Spergel et al. 2007) in which  $H_0 = 73.2 \text{ km s}^{-1} \text{ Mpc}^{-1}$ ,  $\Omega_m = 0.238$ , and  $\Omega_\Lambda = 0.762$ .

## 2. OBSERVATIONS

### 2.1. Target Selection

Recent years have witnessed an abundance of methods for locating galaxies in the redshift range  $z \sim 2$ –3. These methods include optical ( $U_nGR$ ) color selection (e.g., Steidel et al. 2003, 2004), NIR  $BzK$  (Daddi et al. 2004) and  $J-K$  (Franx et al. 2003) color selection, selection by submillimeter flux density (Chapman et al. 2005), and Ly $\alpha$  emission surveys (e.g., Martin et al. 2008, and references therein). Of these samples, those arising from the optical color selection are perhaps the most well studied and account for most of the global star formation activity at  $z \sim 2$ –3 (Reddy et al. 2005). As described in detail by Adelberger et al. (2004), the  $U_nGR$  selection technique represents a generalized version of the Lyman-break technique employed by Steidel et al. (2003) to identify rapidly star-forming galaxies at  $z \sim 3$  on the basis of their strong 912 Å Lyman break, redshifted into the  $U_n$  bandpass. In this paper, we focus primarily on this  $U_nGR$  sample, and particularly on those galaxies in the redshift range  $z = 1.8$ –2.6 (i.e., the “BX” galaxy sample of Steidel et al. 2004). While initial identification of these galaxies was based upon photometric preselection, extensive rest-UV spectroscopic follow-up work has derived precise redshifts for all galaxies in our target sample.

The galaxies selected in this manner are typically bright and actively forming stars, with mean extinction-corrected SFRs  $\sim 30 M_\odot \text{ yr}^{-1}$  (see discussion by Erb et al. 2006b), and SFR surface densities similar to those observed in local starburst galaxies (e.g., Kennicutt et al. 1998b). The resulting winds from supernovae and massive stars drive energetic ( $\sim$ a few hundred  $\text{km s}^{-1}$ ; C. C. Steidel et al. 2009, in preparation) large-scale outflows into the IGM surrounding these galaxies, creating the ubiquitous blueshifted interstellar absorption features observed in rest-frame UV spectra (e.g., Pettini et al. 2002; Shapley et al. 2003), and the corresponding redshifts of the resonantly scattered Ly $\alpha$  emission line (Verhamme et al. 2008). With the aid of deep NIR (e.g., Erb et al. 2006c) and mid-IR (e.g., Shapley et al. 2005b; Papovich et al. 2006; Reddy et al. 2006b, and references therein) photometry, stellar population modeling suggests that galaxies at  $z \sim 2$ –3 span a broad range of stellar masses and evolutionary states.

Individual galaxies selected for study were drawn from this pool of available targets subject to a variety of criteria. Some targets were deliberately selected for their young stellar population ages and correspondingly small stellar masses, some for their old ages and large stellar masses, and some for other reasons including complex or multicomponent rest-UV morphologies (Law et al. 2007b), strong detections in H $\alpha$  narrowband surveys (Q1700-BX710 and Q1700-BX763), unusual spectral features, or previous acquisition of long-slit kinematic data. Given the relatively shallow OSIRIS  $K$ -band sensitivity limit ( $\text{SFR}_{\text{lim}} \sim 1 M_\odot \text{ yr}^{-1} \text{ kpc}^{-2}$  in 2 hr of integration; Law et al. 2007a) however, the most common criterion applied was preferential selection of those galaxies for which previous long-slit spectroscopy (Erb et al. 2006b) indicated nebular line fluxes

<sup>7</sup> One galaxy presented by Förster Schreiber et al. (2006) was observed with the aid of AO, as were two of the five main galaxies discussed by Genzel et al. (2008).

$\gtrsim 5 \times 10^{-17} \text{ erg s}^{-1} \text{ cm}^{-2}$ . We discuss the nature of our final target sample further in Section 5.1.

Additional physical constraints require that there be a suitably bright ( $R \lesssim 17$ ) star within  $\sim 60''$  of each galaxy to use as a tip-tilt (TT) reference for the LGSAO system,<sup>8</sup> and that the wavelength of redshifted line emission falls between the strong spectroscopically unresolved night-sky OH emission features that dominate the NIR background, and avoids wavelengths of extremely strong telluric absorption bands. The first of these constraints will not systematically bias the resulting sample given its reliance only on the distribution of nearby stars, while the second imposes blackout “windows” in redshift space, the most significant of which spans  $z \sim 2.6\text{--}2.9$ . The final target sample is listed in Table 1 and includes 24 galaxies in nine distinct fields distributed widely across the sky. Of the 24 galaxies observed, 13 galaxies (distributed amongst seven fields) have significant detections while an additional two (Q1623-BX455 and Q2343-BX587) are too poorly detected to merit inclusion in our analysis.

## 2.2. Observational Technique

Observations were performed using the OSIRIS (Larkin et al. 2006) integral-field spectrograph in combination with the Keck II LGSAO system during six observing runs between 2006 June and 2008 September. The majority of these sessions followed the basic observing scheme described in Section 2.1 of Law et al. (2007a), to which we refer the reader for a detailed description of our approach. In brief, we observed the target galaxies in narrowband filters (bandwidth  $\sim 0.1 \mu\text{m}$ ) corresponding to the wavelength of either  $H\alpha$  or  $[\text{O III}]\lambda 5007$  (hereafter  $[\text{O III}]$ ) emission lines using the 50 mas lenslet sampling scale with 900 s individual exposures. Given the redshift range of most of our target galaxies ( $z \sim 2\text{--}2.5$ ),  $H\alpha$  is redshifted into the  $K$  band and we generally choose to observe this emission line since the quality of the LGSAO correction is highest at longer wavelengths. At wavelengths longer than  $\sim 2.26 \mu\text{m}$ , however, the thermal continuum background seen by OSIRIS becomes comparable to that of the atmospheric OH lines, significantly degrading the quality of the observational data. We therefore observe  $[\text{O III}]$  emission in either the  $H$  or  $K$  bands as necessary for some galaxies (e.g., Q1623-BX543 and DSF2237a-C2). The observational configuration for each of our target galaxies is detailed in Table 1.

During a typical observing sequence we first acquire a brief ( $\sim 60$  s) observation of our TT reference star in order to center our pointing and provide both a point-spread function (PSF) and flux calibration reference. When possible, we obtained another observation of the TT reference star at the end of our integration on a given galaxy in order to bracket the science observations and measure any changes in the PSF. We offset from the TT star to the target galaxy using precise offsets measured from deep ( $\sim 10$  hr) ground-based optical and/or *Hubble Space Telescope* (*HST*) Advanced Camera for Surveys (ACS) imaging data (where available). Each galaxy was observed in pairs of 900 s exposures dithered within the field of view, typically by  $\sim 1''.4$  along the long axis. This dithering maximizes our on-source integration time but effectively halves our useful field

of view to  $\sim 1'' \times 1''.5$  (still significantly larger than the typical galaxy, see discussion by Law et al. 2007b). Each exposure pair was repeated with small  $\sim 50$  mas dithers for a total of between 1800 and 12,600 s of integration. Total integration times for each object (Table 1) were dictated by observational availability and the need to obtain sufficient integration to ensure high-quality detections. It was typically possible to confirm detection of a given galaxy in the difference of two 900 s exposures, allowing us to determine in real-time the targets that were likely to produce the best results given sufficient integration. With some notable exceptions (e.g., Q2343-BX389) deeper integrations were not performed if a given galaxy was undetected within 1–2 hr.

## 2.3. Data Reduction and Flux Calibration

Data reduction was performed using a combination of OSIRIS pipeline and custom IDL routines described in Section 2.2 of Law et al. (2007a) which produce a composite, three-dimensional data cube (consisting of two image dimensions and one spectral dimension) for each target galaxy. Given the multiyear baseline over which our observations were obtained, the reduction algorithms have evolved over time to reflect the changing performance characteristics of OSIRIS. The most significant modification was introduced for data obtained in 2007 June (i.e., for our observation of galaxies HDF-BX1564 and Q1623-BX502) which were affected by an imperfect focus within OSIRIS resulting in a PSF slightly elongated along an axis roughly 45 deg to the lenslet grid. This was corrected by implementing a CLEAN-type algorithm (e.g., Högbom 1974) to deconvolve the elongated PSF and replace it with a more typical circular PSF.

As described by Law et al. (2007a) the composite data cube for each galaxy is subsampled by a factor of 2 in each spatial dimension and convolved with a Gaussian kernel in order to increase the signal-to-noise ratio (S/N) of the spectrum in each spatial pixel (spaxel). The width of this Gaussian is chosen as required to produce the highest quality smoothed data cube without significantly inflating the PSF delivered by the LGSAO system. We typically chose an FWHM of 80 mas, although for some extremely low surface brightness galaxies (e.g., HDF-BX1564) we increased this smoothing to  $\sim 200$  mas in order to increase the S/N at the cost of spatial resolution. The effective width of the PSF (as measured from the TT star) before and after this smoothing is given for all galaxies in Table 1. For one galaxy (HDF-BX1564) we also smooth the spectrum of each lenslet in the wavelength domain by a kernel of FWHM 5 Å to better distinguish the faint emission feature from the surrounding noise. We note that while these algorithms are largely automated, the details for each observation are carefully optimized to produce the highest possible quality final products.

Raw composite spectra of each galaxy (shown in Figure 1) were obtained by summing into a single spectrum the data from all spaxels in a box encompassing the nebular emission morphology, thereby sampling both bright and faint emission regions. This raw spectrum is calibrated using a telluric transmission spectrum of the night sky to normalize the throughput as a function of wavelength. This calibration spectrum is determined directly from observations of bright telluric standard stars for data obtained in 2008 June/September, and from the OSIRIS + Keck LGSAO system + atmospheric models of Law et al. (2006) for all previous data (see discussion in Law et al. 2007a). The absolute flux calibration of the corrected spectra is determined by matching extracted spectra of the TT stars to IR photometry

<sup>8</sup> The theoretical sky coverage of the Keck LGSAO system (see, e.g., <http://www2.keck.hawaii.edu/optics/lgsao/performance.html>) is  $\sim 60\%$ , ranging from almost 100% near the Galactic plane to  $\sim 20\%$  or less near the Galactic poles and in particularly sparse fields such as the Hubble Deep Field. Generally, we found that  $\sim 70\%$ – $80\%$  of our desired targets were close enough to a bright star to be observed with the LGSAO system.

**Table 1**  
Observing Details

Galaxy	$z_{\text{neb}}^{\text{a}}$	R.A. (J2000.0)	Decl. (J2000.0)	Observing Run	Exposure Time <sup>b</sup> (s)	Filter	Em. Line <sup>c</sup>	Scale (mas)	$\theta_{\text{PSF}}^{\text{d}}$ (mas)
Detections									
Q0449-BX93	2.0067	04:52:15.417	-16:40:56.88	2006 Oct	16200	Kn1	H $\alpha$	50	115/170
Q1217-BX95	2.4244	12:19:28.281	+49:41:25.90	2008 Jun	6300	Kn4	H $\alpha$	50	95/135
HDF-BX1564	2.2228	12:37:23.470	+62:17:20.00	2007 Jun	3600	Kn2	H $\alpha$	50	150/290
Q1623-BX453	2.1820	16:25:50.854	+26:49:31.28	2006 Jun	9000	Kn2	H $\alpha$	50	70/140
Q1623-BX502	2.1557	16:25:54.385	+26:44:09.30	2007 Jun	9900 <sup>e</sup>	Kn2	H $\alpha$	50	195/220
Q1623-BX543	2.5211	16:25:57.707	+26:50:08.60	2008 Jun	11700	Hn5	[O III]	50	95/145
Q1700-BX490	2.3958	17:01:14.830	+64:09:51.69	2008 Jun	11700	Kn4	H $\alpha$	50	75/125
Q1700-BX710	2.2947	17:01:22.128	+64:12:19.21	2006 Jun	5400	Kn3	H $\alpha$	50	70/140
Q1700-BX763	2.2919	17:01:31.463	+64:12:57.67	2008 Jun	12600	Kn3	H $\alpha$	50	75/190
DSF2237a-C2	3.3172	22:40:08.298	+11:49:04.89	2006 Jun	5400	Kn3	[O III]	50	70/140
Q2343-BX418	2.3053	23:46:18.582	+12:47:47.77	2008 Jun	6300	Kn3	H $\alpha$	50	100/150
Q2343-BX513	2.1082	23:46:11.133	+12:48:32.54	2006 Oct	12600	Kn1	H $\alpha$	50	110/165
Q2343-BX660	2.1739	23:46:29.447	+12:49:45.93	2008 Sep	10800	Kn2	H $\alpha$	50	90/140
Nondetections									
Q0100-BX210	2.279 <sup>f</sup>	01:03:11.996	+13:16:18.32	2006 Oct	1800 <sup>e</sup>	Kn3	H $\alpha$	50	120
				2007 Sep	3600 <sup>e</sup>	Hn3	[O III]	50	90
				2007 Sep	5400 <sup>e</sup>	Kn3	H $\alpha$	50	120
HDF-BX1311	2.4843 <sup>f</sup>	12:36:30.514	+62:16:26.00	2007 Jun	4500 <sup>e</sup>	Kn4	H $\alpha$	50	140
HDF-BX1439	2.1865 <sup>f</sup>	12:36:53.660	+62:17:24.00	2008 Jun	2700	Kn2	H $\alpha$	50	70
				2008 Jun	7200 <sup>e</sup>	Kn2	H $\alpha$	100	80
Q1623-BX455 <sup>i</sup>	2.4079	16:25:51.664	+26:46:54.60	2008 Jun	5400	Kn4	H $\alpha$	50	85
				2007 Sep	3600	Hn4	[O III]	50	70
Q1623-BX663	2.4333 <sup>f</sup>	16:26:04.586	+26:47:59.80	2007 Jun	5400 <sup>e</sup>	Kn4	H $\alpha$	50	100
Q1700-BX563	2.292 <sup>g</sup>	17:01:15.875	+64:10:26.15	2007 Jun	1800 <sup>e</sup>	Kn3	H $\alpha$	50	210
Q1700-BX691	2.1895 <sup>f</sup>	17:01:06.117	+64:12:09.70	2006 Jun	10800 <sup>h</sup>	Kn2	H $\alpha$	50	...
				2007 Jun	5400 <sup>e</sup>	Kn2	H $\alpha$	50	200
Q2206-BX102	2.2104 <sup>f</sup>	22:08:50.751	-19:44:08.24	2007 Sep	5400	Kn2	H $\alpha$	50	90
Q2343-BX389	2.1716 <sup>f</sup>	23:46:28.911	+12:47:33.90	2007 Jun	8100 <sup>e</sup>	Kn2	H $\alpha$	50	160
Q2343-BX442	2.1760 <sup>f</sup>	23:46:19.362	+12:48:00.10	2007 Sep	9000 <sup>e</sup>	Kn2	H $\alpha$	50	140
Q2343-BX587 <sup>i</sup>	2.2429	23:46:29.192	+12:49:03.71	2006 Oct	5400	Kn3	H $\alpha$	50	105

**Notes.**

<sup>a</sup> Vacuum heliocentric redshift of primary nebular emission line.

<sup>b</sup> Total observing time, mean value for detected sources was  $\sim 2$  hr.

<sup>c</sup> Primary targeted emission line.

<sup>d</sup> FWHM of the  $K$ -band PSF (mas) during on-axis TT star observation (before/after spatial smoothing, respectively).

<sup>e</sup> Poor observing conditions.

<sup>f</sup> Redshifts estimated from NIRSPEC spectra.

<sup>g</sup> Redshift estimated from rest-UV spectrum.

<sup>h</sup> Individual exposures were each 300 s.

<sup>i</sup> Galaxy detected, but quality too poor for analysis.

given in the Two Micron All Sky Survey (2MASS) Point-Source Catalog. We note that this method differs from that adopted by Law et al. (2007a), and slight differences from their calibration are to be expected.

The largest single uncertainty in the flux calibration of these data arises from the nature of the LGS AO PSF, which can vary both with isoplanatic angle and (rapidly) with time, resulting in significant fluctuations in the percentage of total light residing in the AO-corrected core of the PSF. These fluctuations are poorly understood, and correlated primarily with midlevel atmospheric turbulence not well corrected by the AO system. In addition, low surface brightness or extremely broad spectral features may be missed entirely (see discussion in Section 5.1), leading to an underestimate of the total flux from galaxies with appreciable flux in such regions. Given the uncertainties in our bootstrapped flux calibration, we estimate that the systematic flux uncertainty for any given source is  $\sim 30\%$  (see also discussion in Law et al. 2007a).

In Table 2, we list the [O III], H $\alpha$ , and [N II] emission-line fluxes of each galaxy (with uncertainties based on the noise present in the underlying spectra after subtraction of Gaussian models for the identifiable emission components<sup>9</sup>) along with estimates of the oxygen abundance based on the Pettini & Pagel (2004) calibration of the  $N2 = F_{[\text{N II}]} / F_{\text{H}\alpha}$  relation. Most of these fluxes are about half the aperture-corrected values determined from the previous long-slit NIRSPEC spectroscopy (Erb et al. 2006b). One possible explanation for this discrepancy may be that the factor of 2 aperture correction used to calibrate the NIRSPEC data could overestimate slit losses (particularly for the most compact galaxies), resulting in erroneously high flux estimates. Alternatively, this may also be due to low surface brightness emission which OSIRIS is not sufficiently sensitive to detect.

<sup>9</sup> Residual features at the emission-line wavelength (after subtraction of the Gaussian model profile) are generally indistinguishable from the noise in the rest of the spectrum.

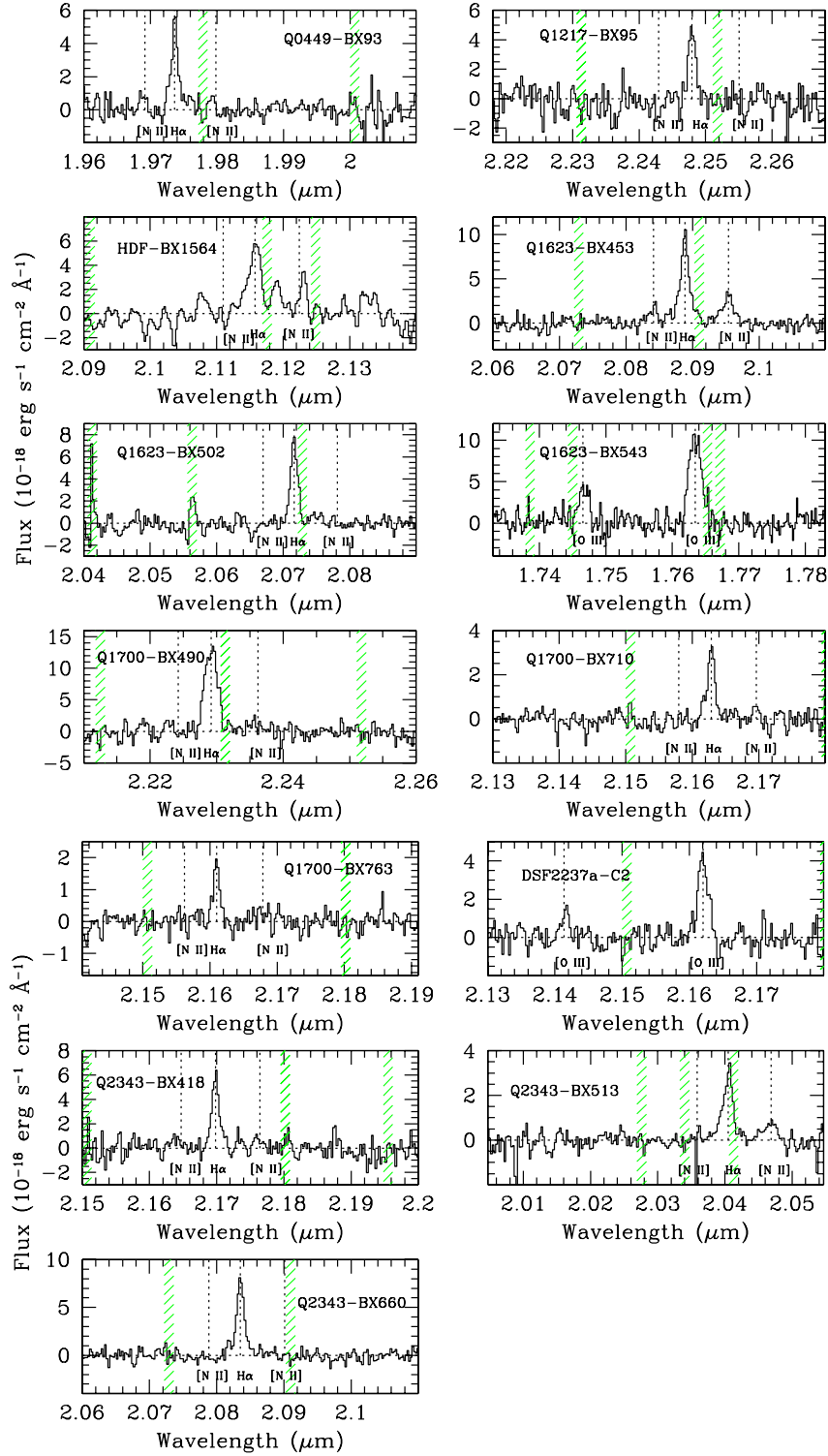


**Figure 1.** OSIRIS spectra integrated over the spatial extent of each galaxy. The vertical dashed lines indicate the fiducial locations of nebular emission lines based on the systemic redshift. The hashed green regions indicate the locations of strong atmospheric OH emission features which can give rise to strong residuals in the spectra.

(A color version of this figure is available in the online journal.)

Total nebular emission-line luminosity is calculated from these fluxes assuming a standard cosmological model and correcting for extinction derived from stellar population models (Section 3.2) using a Calzetti et al. (2000) attenuation law

modified as described by Erb et al. (2006c).<sup>10</sup> We convert this extinction-corrected luminosity to an H $\alpha$  SFR using the

<sup>10</sup>  $E(B - V)$  ranges from 0.005 to 0.370.

**Table 2**  
Nebular Line Fluxes

Galaxy	$\lambda_{\text{neb}}^{\text{a}}$ (Å)	$z_{\text{neb}}^{\text{b}}$	$F_{\text{H}\alpha}^{\text{c}}$	$F_{\text{DKE}}^{\text{d}}$	$F_{[\text{O III}]^{\text{c}}}$ ( $\lambda 5007$ )	$L_{\text{neb}}^{\text{e}}$ ( $10^{42}$ erg s $^{-1}$ )	$F_{[\text{O III}]^{\text{c}}}$ ( $\lambda 4960$ )	$F_{[\text{N II}]^{\text{c}}}$ ( $\lambda 6549$ )	$F_{[\text{N II}]^{\text{c}}}$ ( $\lambda 6585$ )	$12 + \log(\text{O}/\text{H})^{\text{f}}$
Q0449-BX93	19737.8	2.0067	$6.8 \pm 0.2$	...	...	$3.0 \pm 0.1$	...	$1.3 \pm 0.4$	$0.8 \pm 0.3$	$8.37 \pm 0.09$
Q1217-BX95	22479.6	2.4244	$6.5 \pm 0.4$	...	...	$6.4 \pm 0.4$	...	$\leq 1.2$	$\leq 1.2$	$\leq 8.48$
HDF-BX1564	21156.7	2.2228	$9.7 \pm 0.8$	$17.2 \pm 1.4$	...	$7.0 \pm 0.4$	...	$\leq 1.5$	$3.9 \pm 0.5$	$8.67 \pm 0.04$
Q1623-BX453	20888.3	2.1820	$16.4 \pm 0.4$	$27.6 \pm 0.4$	...	$12.8 \pm 0.3$	...	$3.0 \pm 0.4$	$6.5 \pm 0.4$	$8.67 \pm 0.02$
Q1623-BX502	20715.8	2.1557	$10.0 \pm 0.2$	$26.4 \pm 0.8$	...	$5.3 \pm 0.1$	...	$\leq 0.7$	$\leq 0.7$	$\leq 8.24$
Q1623-BX543	17634.4	2.5211	...	$17.2 \pm 1.4$	$25.0 \pm 0.5$	$42.5 \pm 0.8$	$8.0 \pm 0.5$	...	...	...
Q1700-BX490	22291.8	2.3958	$31.6 \pm 0.8$	$35.4 \pm 1.2$	...	$34.6 \pm 0.9$	...	$\leq 2.4$	$\leq 2.4$	$\leq 8.26$
Q1700-BX710	21628.4	2.2947	$4.5 \pm 0.2$	...	...	$3.4 \pm 0.2$	...	$\leq 0.6$	$0.6 \pm 0.2$	$8.40 \pm 0.08$
Q1700-BX763	21609.8	2.2919	$2.2 \pm 0.3$	...	...	$1.3 \pm 0.2$	...	$\leq 0.9$	$0.3 \pm 0.3$	$8.41 \pm 0.25$
DSF2237a-C2	21621.8	3.3172	...	...	$7.9 \pm 0.4$	$16.8 \pm 0.9$	$2.0 \pm 0.3$	...	...	...
Q2343-BX418	21698.2	2.3053	$8.2 \pm 0.4$	$16.0 \pm 0.4$	...	$3.8 \pm 0.2$	...	$\leq 1.2$	$\leq 1.2$	$\leq 8.42$
Q2343-BX513	20404.3	2.1082	$5.4 \pm 0.2$	$20.2 \pm 0.8$	...	$2.9 \pm 0.1$	...	$\leq 0.6$	$1.8 \pm 0.2$	$8.63 \pm 0.03$
Q2343-BX660	20835.4	2.1739	$11.2 \pm 0.2$	$18.8 \pm 0.8$	...	$4.2 \pm 0.1$	...	$\leq 0.6$	$\leq 0.6$	$\leq 8.18$

#### Notes.

<sup>a</sup> Vacuum heliocentric wavelength of primary nebular emission: [O III]  $\lambda 5007$  for DSF2237a-C2 and Q2343-BX415, [N II] for Q1623-BX455, H $\alpha$  for all others.

<sup>b</sup> Heliocentric redshift of primary nebular emission line.

<sup>c</sup> Emission-line flux in units of  $10^{-17}$  erg s $^{-1}$  cm $^{-2}$ . Uncertainties quoted are  $1\sigma$  and based on random errors, global systematic uncertainty is  $\sim 30\%$ . Limits represent  $3\sigma$  limits.

<sup>d</sup> H $\alpha$  emission-line flux observed by Erb et al. (2006c) (includes a factor of 2 correction for aperture losses).

<sup>e</sup> Extinction-corrected primary nebular emission-line luminosity (H $\alpha$  or [O III]). Uncertainties quoted are based on random errors, global systematic uncertainty is  $\sim 30\%$ .

<sup>f</sup> Oxygen abundance using the N2 calibration from Pettini & Pagel (2004).

Kennicutt et al. (1994) calibration,

$$\text{SFR} (M_{\odot} \text{ yr}^{-1}) = \frac{L(\text{H}\alpha)}{1.26 \times 10^{41} \text{ erg s}^{-1}} \times 0.56, \quad (1)$$

where the factor of 0.56 converts to the Chabrier (2003) initial mass function (IMF). For those two galaxies observed in [O III] instead of H $\alpha$  we either assume that  $\frac{L_{\text{H}\alpha}}{L_{[\text{O III}]}} = 1$  (Q1623-BX543, for which the actual flux ratio is unknown) or adopt  $\frac{L_{\text{H}\alpha}}{L_{[\text{O III}]}} = 0.52$  (DSF2237a-C2, see discussion in Law et al. 2007a). We also list the central wavelength of the primary observed emission feature in each spectrum. Systemic redshifts are determined by dividing these wavelengths by the rest-frame vacuum wavelengths of H $\alpha$  and [O III] (i.e., 6564.614 Å and 5008.239 Å, respectively) and correcting for the heliocentric motion of the Earth at the date, time, and direction of observation (calculated using the IRAF *rvcorrect* algorithm). We do not include fainter [N II] or [O III]  $\lambda 4960$  in our systemic redshift calculations as these features are generally too weak to improve the redshift fit.

Kinematic data were extracted from the oversampled composite data cubes using custom IDL routines to fit Gaussian profiles to the spectrum at each spatial location, thereby obtaining maps of the emission-line flux, wavelength centroid, and spectral FWHM across each galaxy. This information is converted to maps of the velocity relative to the systemic redshift and the velocity dispersion (with the instrumental resolution [ $R \sim 3600$ ] subtracted off in quadrature) as shown in Figure 2. As discussed by Law et al. (2007a), the quality of these maps is improved considerably by the spatial smoothing described above, and by excluding any fits which are either unphysical or for which the data had inadequate S/N.

## 3. RESULTS

### 3.1. Morphologies

As demonstrated by numerous authors (e.g., Abraham et al. 1996; Conselice et al. 2005; Elmegreen et al. 2005; Lotz et al. 2006; Law et al. 2007b) the morphological structure of galaxies at redshift  $z \gtrsim 2$  is highly irregular and frequently composed of multiple spatially separated components when observed in the rest-frame UV. It is worthwhile exploring the similarity between such rest-UV morphologies and those of the ionized gas. Given the extremely faint nature of these galaxies, we produce maps of the ionized gas morphology (Figure 2, left-hand panels) by summing spectral channels within  $1\sigma$  of the peak emission wavelength at each oversampled spatial pixel meeting the S/N criteria described in Section 3.3. Such a “tunable” narrowband filter for each position in the galaxy minimizes the contribution of noise to the flux map.

Following the method outlined by Abraham et al. (2007) we define a segmentation map for each galaxy using a quasi-Petrosian isophotal cut ( $\eta = 0.2$ ) which is independent of morphology. Using this segmentation map we calculate a variety of morphological statistics including the Gini coefficient  $G$  (a measure of the curve of growth of the light distribution, see discussion by Abraham et al. 2003), the multiplicity parameter  $\Psi$  (a measure of the number of components of the light distribution, see Law et al. 2007b), the second-order moment  $M_{20}$  of those pixels constituting the top 20% of the total flux (Lotz et al. 2004), the total luminous area  $I$  and effective radius  $r$  corrected for the PSF as described in Law et al. (2007a), and the distance  $d_{2c}$  between individual components (for galaxies which have spatially separated pieces). These measurements are given in Table 3.

We note, however, that it is difficult to compare these values directly to rest-UV morphological data presented by Lotz

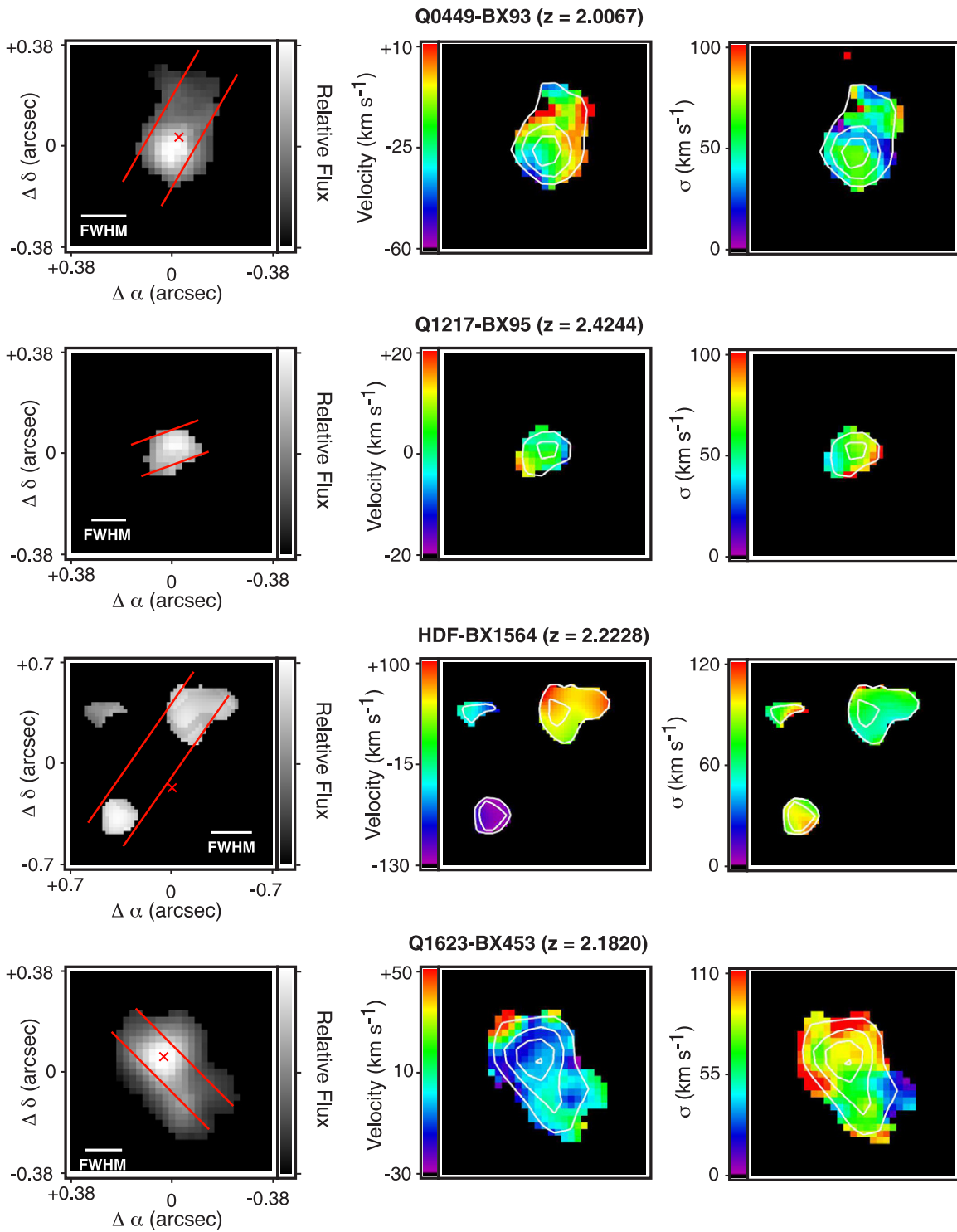


**Figure 2.** OSIRIS maps of nebular emission ([O III] for Q1623-BX543 and DSF2237a-C2, H $\alpha$  for all others). Panels represent (left to right) flux, relative velocity, and velocity dispersion maps. Individual pixels measure 25 mas, the total field of view varies from target to target as needed to contain the emission-line regions. The FWHM of the PSF (after smoothing described in Section 2.3) is indicated in the left-hand panel for each galaxy. Contours represent linear intervals in line flux density. All images are presented in a standard orientation with north up, and east left. The red lines indicate the “slits” used to extract the one-dimensional velocity curves shown in Figure 5. The red  $\times$  marks indicate the location of peak [N II] emission (when present). Lone pixels are likely noise artifacts rather than genuine galaxy features.

et al. (2004, 2006) and Law et al. (2007b) due to systematic differences in the observational data. First (and most important) the quasi-Petrosian isophotal cut simply selects all pixels above our S/N ratio threshold for nearly all of our galaxies since our method of constructing the lowest noise flux maps has artificially eliminated all of the fainter galaxy pixels for which it was not

possible to fit a reliable emission-line spectrum. While this is clearly not ideal from a morphological standpoint, for our lowest surface brightness sources (e.g., HDF-BX1564) this spectral line fitting method and associated S/N cut is frequently the only mechanism by which we can reliably distinguish any features from the background noise at all. Our isophotal cut generally

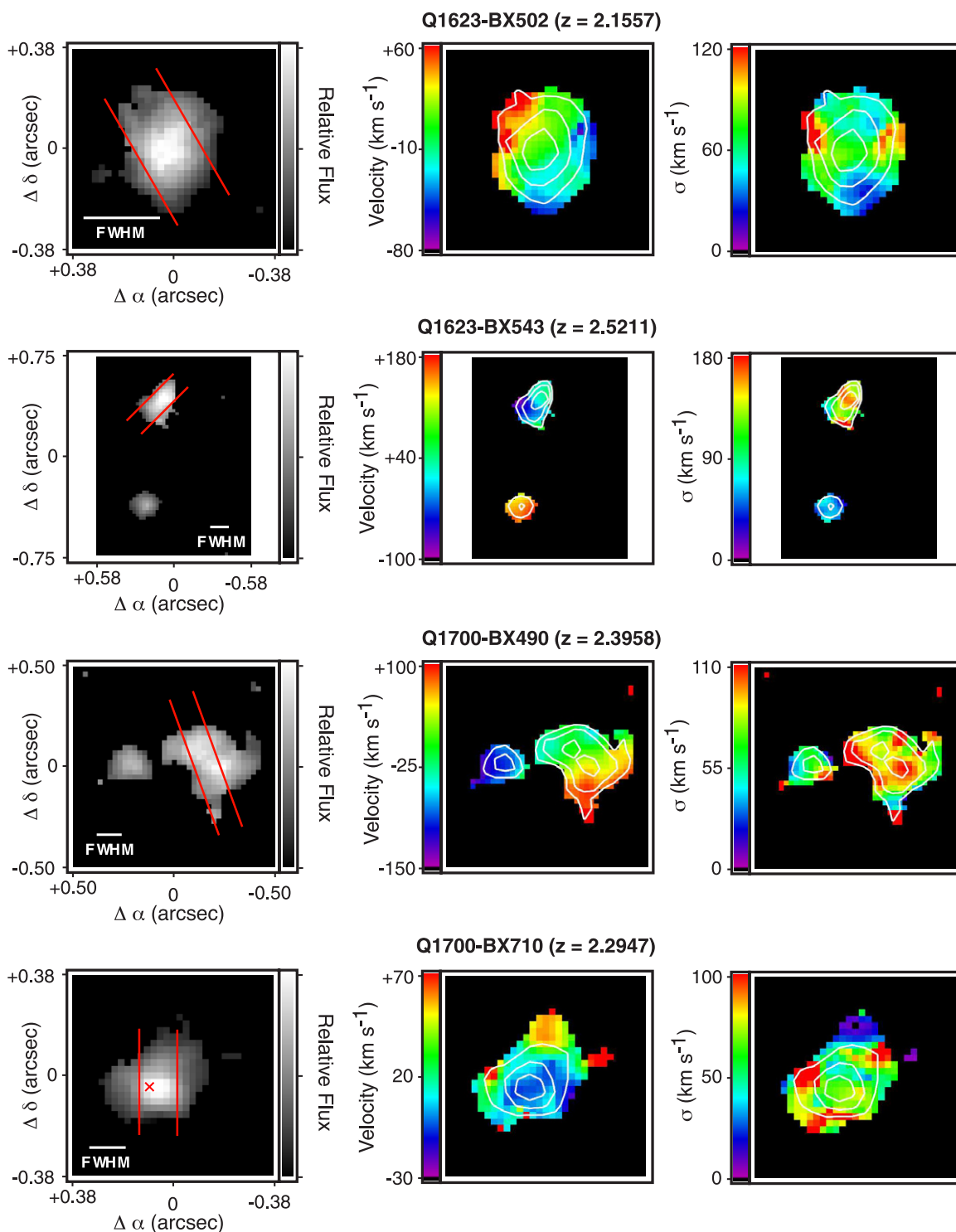


Figure 2. (Continued)

does not reach surface brightness levels as low as those of many narrowband studies; this results in lower values of  $G$  than are normally derived in the rest-frame UV (e.g., Lotz et al. 2004, 2006; Law et al. 2007b) as there is less contrast among pixels in the segmentation map. In contrast, the multiplicity parameter  $\Psi$  is relatively robust to such surface brightness variations and still reliably indicates the presence of multiple components in the light profile. Additionally, many of the galaxies observed are only a few times the size of the observational PSF (which can vary considerably from galaxy to galaxy) which also has

an impact on the numerical classification of the morphology. We therefore recommend that these morphological statistics be interpreted in a relative, rather than absolute, sense.

Four of our target galaxies (HDF-BX1564, Q1700-BX490, Q1700-BX710, and Q1700-BX763) lie in fields for which deep optical imaging data have been obtained with *HST*-ACS. These data in the HDF and Q1700 fields have been described by Law et al. (2007b) and Peter et al. (2007), respectively. The comparative morphologies of *HST*-ACS (i.e., tracing the rest-UV continuum) and OSIRIS H $\alpha$  emission are shown in



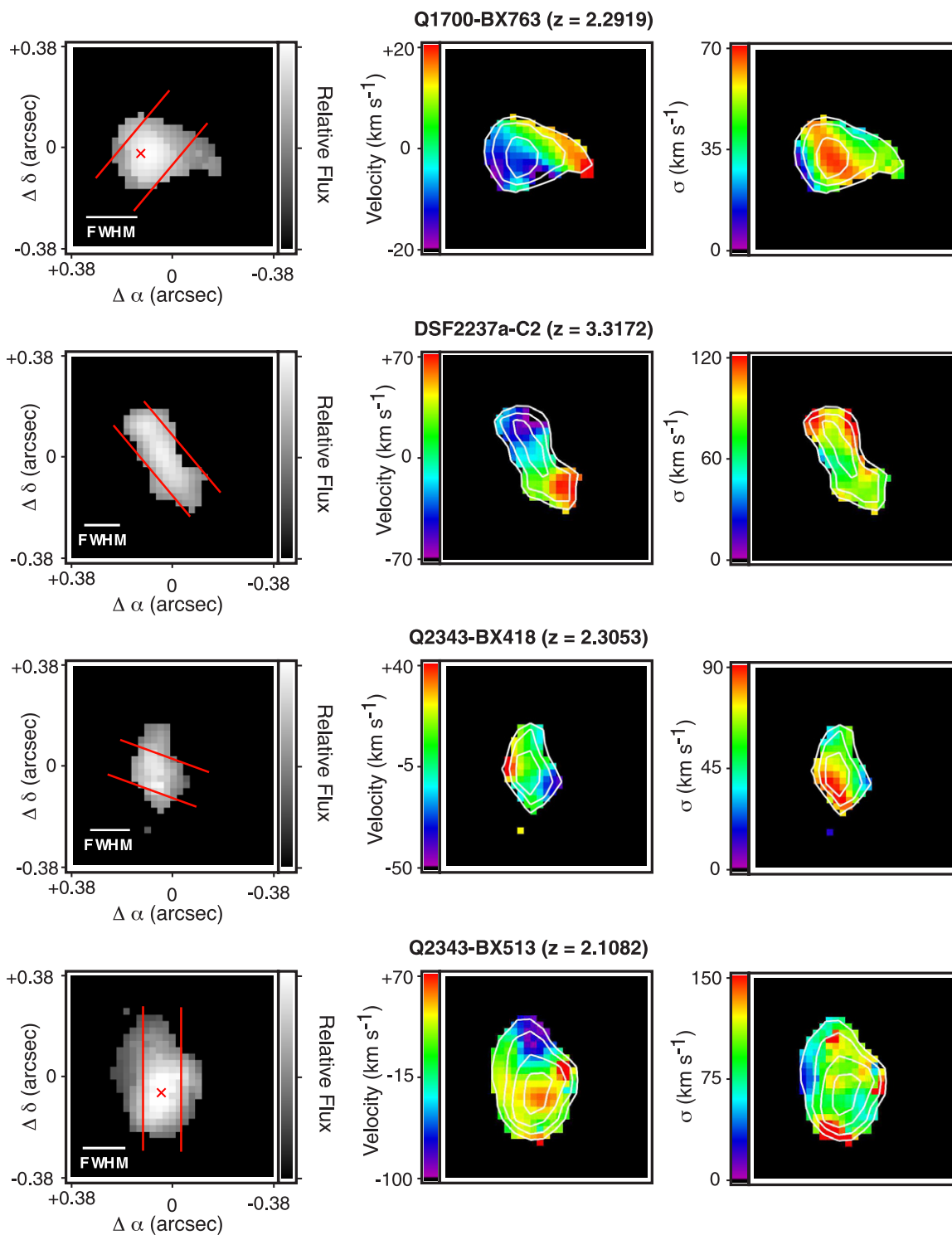


Figure 2. (Continued)

Figure 3. Given the factor of  $\sim 5$  difference between the limiting SFR surface density probed by the *HST*-ACS and OSIRIS data ( $\sim 0.2 M_{\odot} \text{ yr}^{-1} \text{ kpc}^{-2}$  and  $\sim 1 M_{\odot} \text{ yr}^{-1} \text{ kpc}^{-2}$ , respectively; see discussion in Law et al. 2007a) there is generally a good correspondence between the respective morphologies. Due to the extremely narrow field of view of OSIRIS, there are no absolute reference points to which we can calibrate the coordinate solution as our offsets from the TT acquisition star are only reliable to within  $\sim 100$  mas (i.e., comparable to our

PSF) due to various uncertainties resulting from (for example) measuring the coordinates of the TT star, global uncertainties in the coordinate solution of the ground-based imaging data, and the unknown proper motion of the TT stars. It is not possible therefore to reliably align the *HST*-ACS and OSIRIS images to high precision using absolute coordinates alone. Instead, we align the *HST*-ACS contours shown in Figure 3 with the OSIRIS maps “by-eye,” sliding the contours freely until they appear to best overlap the  $H\alpha$  flux data. While this

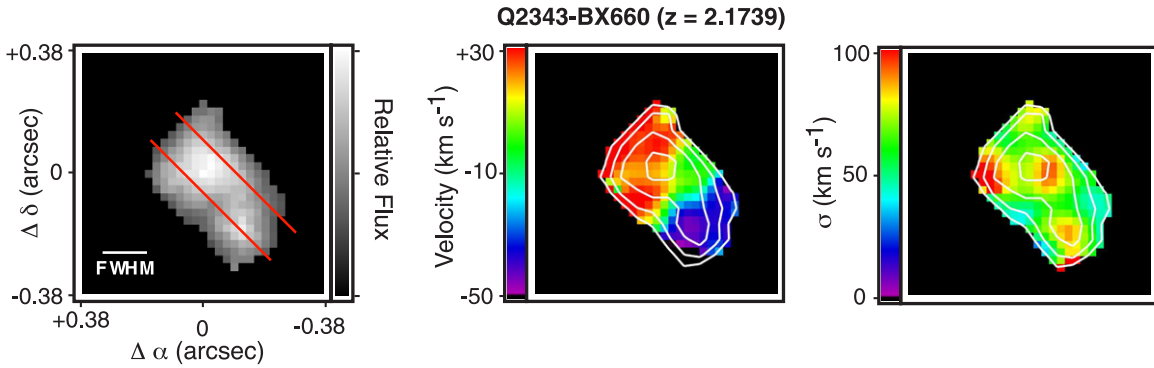


Figure 2. (Continued)

Table 3  
OSIRIS Morphologies

Galaxy	$I^a$ (kpc <sup>2</sup> )	$r^b$ (kpc)	$d_{2c}^c$ (kpc)	$G^d$	$\Psi^e$	$M_{20}$
Q0449-BX93	$5.0 \pm 0.8$	$1.3 \pm 0.1$	...	0.24	1.2	-1.08
Q1217-BX95	$1.0 \pm 0.4$	$0.6 \pm 0.1$	...	0.13	0.8	-0.89
HDF-BX1564	$5.3 \pm 2.1$ (NW) $\leq 3$ (SE)	$1.3 \pm 0.2$ (NW) $\leq 1$ (SE)	7.0	0.10	13.6	-0.51
Q1623-BX453	$6.1 \pm 0.5$	$1.4 \pm 0.1$	...	0.22	1.3	-1.36
Q1623-BX502	$6.2 \pm 1.3$	$1.4 \pm 0.2$	...	0.21	0.7	-1.48
Q1623-BX543	$3.6 \pm 0.5$ (N) $1.5 \pm 0.5$ (S)	$1.1 \pm 0.1$ (N) $0.7 \pm 0.1$ (S)	6.7	0.19	9.7	-1.09
Q1700-BX490	$8.3 \pm 0.4$ (W) $1.6 \pm 0.4$ (E)	$1.6 \pm 0.1$ (W) $0.7 \pm 0.1$ (E)	3.4	0.15	5.8	-1.40
Q1700-BX710	$4.1 \pm 0.5$	$1.1 \pm 0.1$	...	0.23	0.5	-1.51
Q1700-BX763	$3.9 \pm 0.9$	$1.1 \pm 0.1$	...	0.14	1.5	-1.22
DSF2237a-C2	$2.7 \pm 0.4$	$0.9 \pm 0.1$	...	0.17	2.4	-1.16
Q2343-BX418	$2.2 \pm 0.6$	$0.8 \pm 0.1$	...	0.13	1.8	-1.32
Q2343-BX513	$6.2 \pm 0.7$	$1.4 \pm 0.1$	...	0.19	1.1	-1.28
Q2343-BX660	$8.5 \pm 0.5$	$1.6 \pm 0.1$	...	0.18	1.7	-0.99

**Notes.**

<sup>a</sup> Area of nebular emission. Uncertainty represents half the PSF correction. Individual components are identified in parentheses.

<sup>b</sup> Radius of nebular emission. Uncertainty represents half the PSF correction. Individual components are identified in parentheses.

<sup>c</sup> Distance between the two morphological components.

<sup>d</sup> Gini.

<sup>e</sup> Multiplicity.

prohibits us from investigating small discrepancies between the locations of peak emission in isolated single sources, we are still able to compare spatial differences for sources with multiple emission features and the relative shapes of the various emission profiles. We discuss the specific features of individual galaxies in Sections 4.1–4.13 below.

### 3.2. Stellar Population Modeling and Gas Masses

Using our extensive ground-based  $U_nGRJK_s$  and *Spitzer* Infrared Array Camera (IRAC) and Multiband Imaging Photometer for *Spitzer* (MIPS) photometry in the selected survey fields it is possible to construct stellar population models for the spectral energy distributions (SEDs) of the target galaxies. The modeling procedure is described in detail by Shapley et al. (2005a). In brief, we use Bruzual & Charlot (2003) models with a constant SFR (unless otherwise specified), solar metallicity, and a Chabrier (2003) IMF. These models are overplotted on our photometric data in Figure 4 and the individual values for SFR, stellar mass ( $M_*$ ), population age, and extinction are tabulated

in Table 4. As discussed by previous authors (e.g., Shapley et al. 2001, 2005a; Papovich et al. 2001), degeneracies in the stellar population model tend to cancel out with regard to the total stellar mass, meaning that this is typically the best constrained of these parameters. We note that previous modeling of many of these galaxies has been presented by Erb et al. (2006c) and Shapley et al. (2001); the previous models are updated here for consistency and to add *Spitzer* IRAC data where available.

The galaxies for which the poorest fit to the photometry is obtained (HDF-BX1564, Q1623-BX502, Q1623-BX543, and Q2343-BX660) tend to be those with multiple components to the light distribution. In general, however, there is reasonable agreement between the values of SFR derived from SED fitting and those implied by the  $H\alpha$  luminosity (Table 4), although the SED-based estimates tend to be systematically greater than those based on  $H\alpha$ .

We also include in Table 4 estimates of the mass in cold gas of each of our galaxies (and the corresponding gas fraction  $\mu = M_{\text{gas}}/(M_{\text{gas}} + M_*)$ ) determined by Erb et al. (2006c) based on the long-slit NIRSPEC spectroscopy. While it would be possible to use the global Schmidt law (Kennicutt 1998) to calculate new estimates of  $M_{\text{gas}}$  from our observed  $H\alpha$  fluxes, the results of this calculation are sensitive to both  $H\alpha$  flux and the apparent size of the galaxy, which systematically differ between OSIRIS and NIRSPEC due to the different surface brightness thresholds reached by the two spectrographs. We use the Erb et al. (2006c) estimates for consistency in our later (Section 5.2) comparison to other galaxy samples.

### 3.3. Kinematics

As illustrated by Figure 2 (middle panels), galaxies show a mix of velocity fields ranging from largely featureless (Q1623-BX453) to smoothly varying (Q1700-BX490) to extremely complex (Q2343-BX513). In particular, we find that five of our galaxies (Q1623-BX502, Q1623-BX543, Q1700-BX490, DFS2237a-C2, and Q2343-BX418) have velocity fields consistent with rotation-like velocity gradients, six (Q0449-BX93, Q1217-BX95, HDF-BX1564, Q1623-BX453, Q1700-BX710, and Q1700-BX763) consistent with negligible velocity structure, and two (Q2343-BX513 and Q2343-BX660) with velocity structure unlike simple rotation. Additionally, three of our 13 galaxies (HDF-BX1564, Q1623-BX543, and Q1700-BX490) consist of multiple spatially (and kinematically) distinct regions: two of these galaxies display significant kinematic shear in their individual components (Q1623-BX543 and Q1700-BX490) while one does not (HDF-BX1564).

We discuss the kinematics of individual galaxies in detail in Section 4. The single feature common to all of these

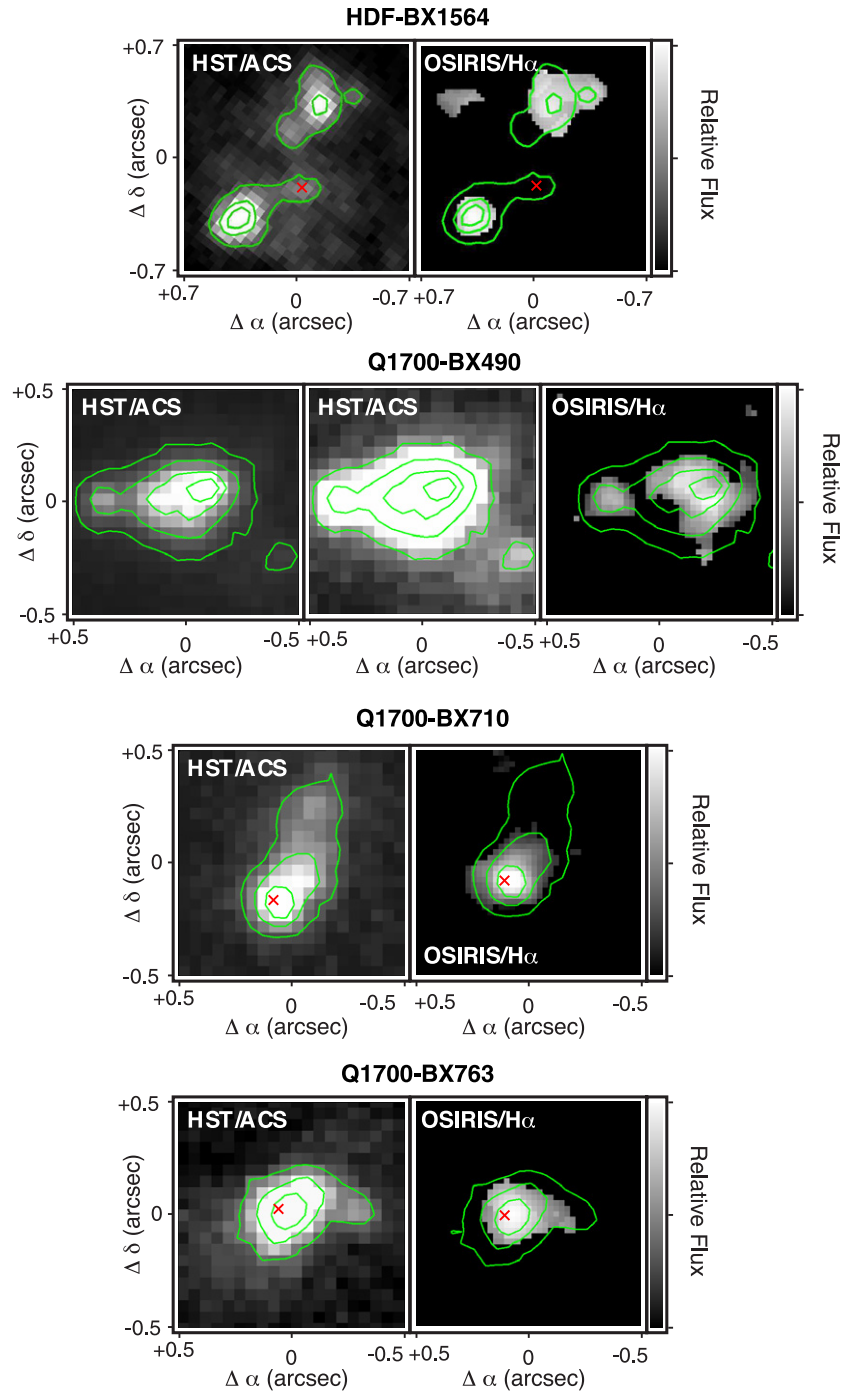


**Figure 3.** Comparison between *HST*-ACS rest-UV continuum morphologies and OSIRIS nebular emission morphologies. In each panel, the gray scale and contours are linear in rest-UV flux density. Two copies of the *HST*-ACS map for Q1700-BX490 are included with different gray scale stretches to best emphasize both bright and extended faint structure. Note that the fields of view for Q1700-BX710 and Q1700-BX763 are slightly larger than those in Figure 2 in order to completely encompass the extended *HST*-ACS morphology. The red  $\times$  marks indicate the centroid of peak [N II] emission (when present). (A color version of this figure is available in the online journal.)

galaxies however is the significant velocity component with no preferred kinematic axis (Figure 2, right-hand panels) which dominates over all coherent kinematic structures. This velocity dispersion may be quantified in two ways. An estimate of the overall velocity dispersion  $\sigma_{\text{net}}$  of a galaxy may be obtained by simply fitting a single Gaussian profile to the spatially integrated spectrum of the entire galaxy (i.e., the spectra shown in Figure 1). This measurement does not distinguish between spatially resolved velocity gradients and small-scale motions

within a given resolution element. While  $\sigma_{\text{net}}$  can provide a reasonable estimate of the dynamical mass using the formula

$$M_{\text{dyn}} = \frac{C\sigma_{\text{net}}^2 r}{G} \quad (2)$$

(where  $C = 5$  for a uniform sphere; see Erb et al. 2006c), it is not an optimal means of determining the intrinsic dispersion of the ionized gas. We therefore also calculate  $\sigma_{\text{mean}}$  which is the

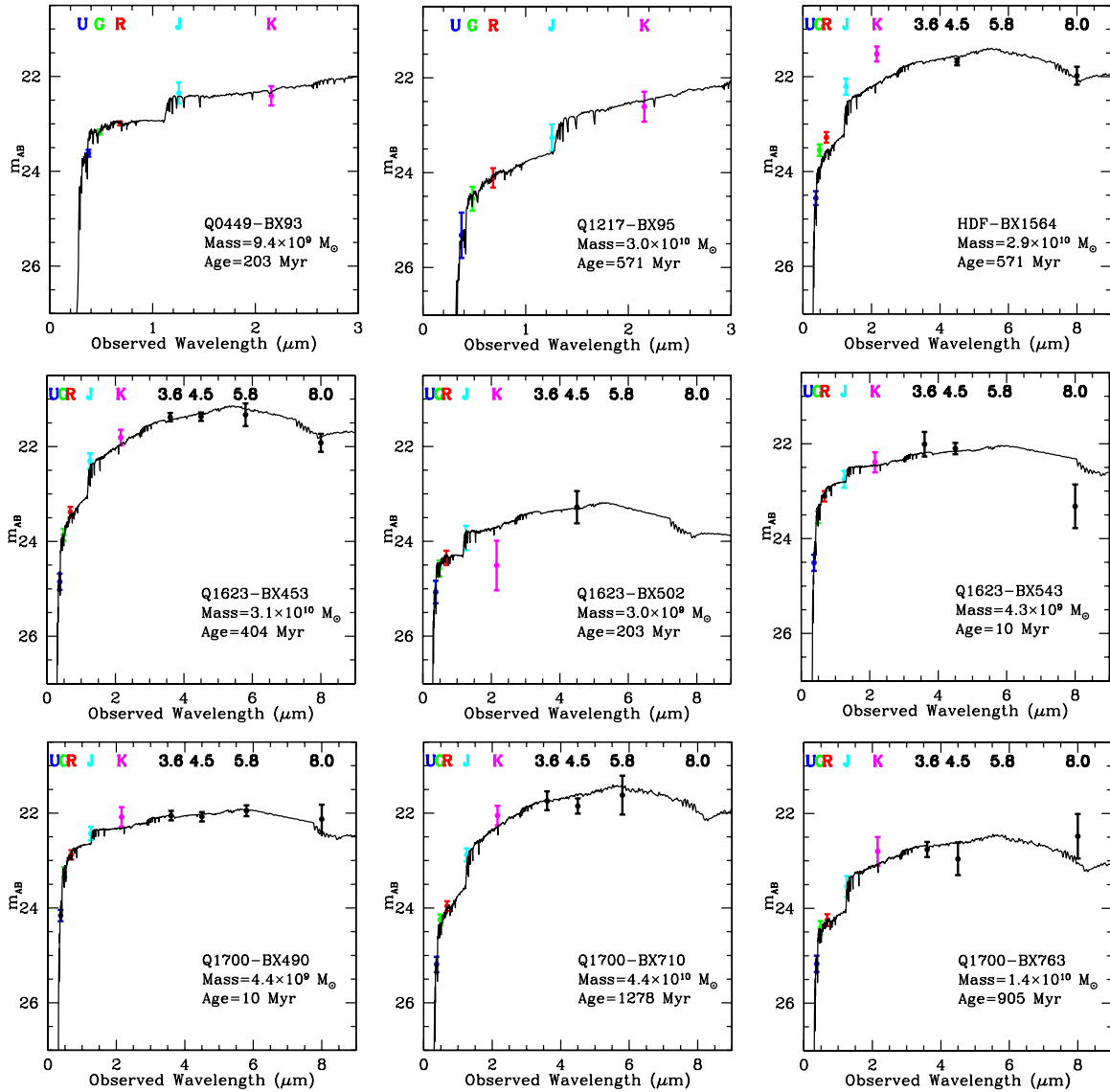


**Figure 4.** Best-fit constant star formation (CSF) model (solid black line) is overlaid against the observed SED for our target galaxies. The colored points represent ground-based optical and NIR photometry; the black points are based on *Spitzer*-IRAC observations. Values given for stellar mass and population age represent the values derived from the best-fit CSF model using a Chabrier (2003) IMF; typical uncertainties are given in Table 4.

(A color version of this figure is available in the online journal.)

flux-weighted mean<sup>11</sup> of the velocity dispersions measured in each individual spaxel (i.e., the “local” velocity dispersion shown in the right-hand panels of Figure 2). This quantity effectively suppresses spatially resolved velocity gradients and provides a more accurate measure of the typical line of sight velocity dispersion at a given location within the galaxy, albeit with some potential bias due to the flux weighting, beam smearing, and finite sampling of the observational data. Values of  $\sigma_{\text{mean}}$  and  $\sigma_{\text{net}}$  are tabulated in Table 5. In the three cases, where the galaxy consists of spatially distinct regions, we calculate values for  $\sigma_{\text{mean}}$  in each of the regions and also measure the kinematic offset  $v_{2c}$  between them. As expected, values of  $\sigma_{\text{mean}}$  are generally consistent with or slightly less than  $\sigma_{\text{net}}$  except for cases where large-scale velocity structure inflates  $\sigma_{\text{net}}$  (e.g. HDF-BX1564).

<sup>11</sup> We adopt a flux-weighted mean rather than a simple mean in order to minimize contamination from the lowest S/N spectra.

We place these descriptive arguments on a firmer numerical footing by constructing one-dimensional velocity curves of each of our target galaxies as shown in Figure 5. These are obtained by extracting spectra from our calibrated data cubes along simulated slits whose width is matched to the spatial resolution of the data, and orientations (indicated by red lines in Figure 2) chosen to maximize the apparent velocity gradient across the galaxy. We define the shear velocity  $v_{\text{shear}}$  as half the maximum difference between any two positions along these pseudo-slits, noting that this will disregard whether the maximum difference occurs between locations at the extreme ends of a galaxy or indeed whether the resulting velocity curves resembles actual rotation in any way. Any apparent trends can easily be confirmed by the inspection of the two-dimensional velocity map (Figure 2).

Ideally, it would be possible to perform detailed kinematic analyses of each of our galaxies (e.g., Shapiro et al. 2008; Genzel et al. 2008; Wright et al. 2009) in order to obtain a set of

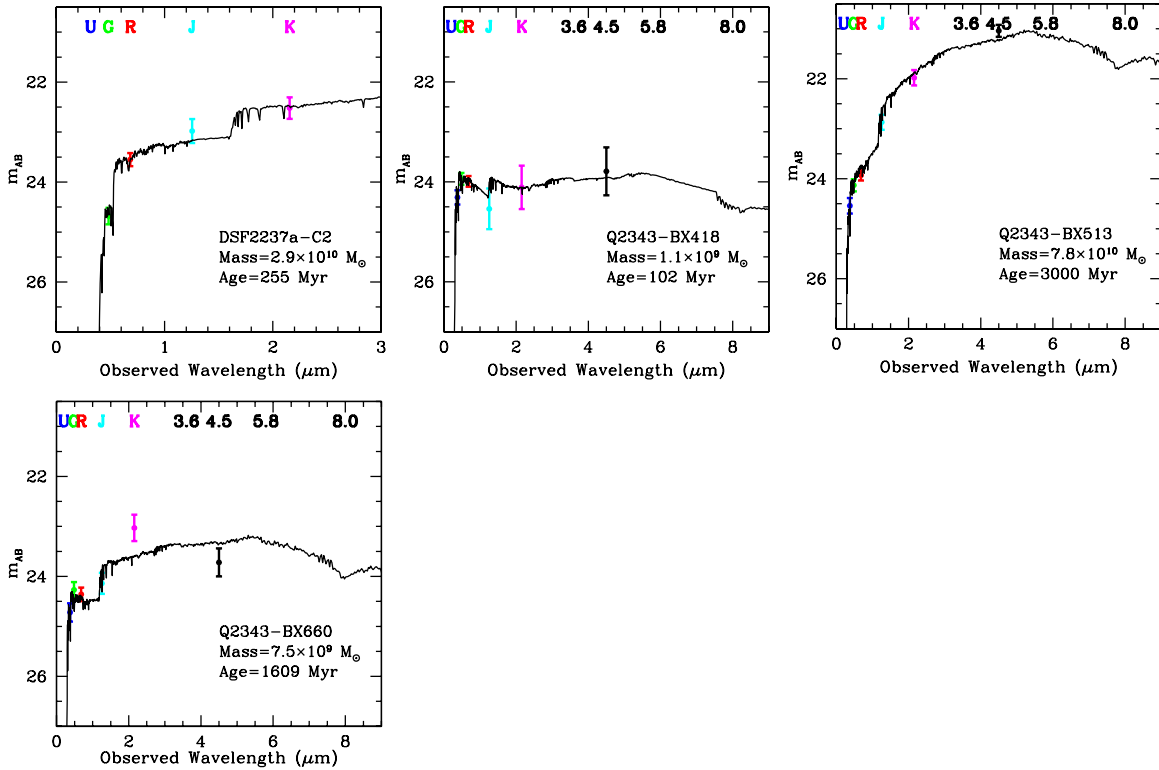


Figure 4. (Continued)

best-fitting models for the light distribution and ionized gas kinematics, along with the dynamical ratio  $v_{\text{disk}}/\sigma_{\text{int}}$  of the model (where  $v_{\text{disk}}$  is the maximum circular speed attained within the galaxy and  $\sigma_{\text{int}}$  is the intrinsic local velocity dispersion). However, the observational data generally do not justify such detailed analyses because the majority of the galaxies do not show concrete evidence (such as spatially resolved velocity shear) to suggest that they might be described by traditional inclined-disk models. Of the five galaxies with smoothly varying velocity gradients consistent with rotation, only two have these gradients aligned with the morphological major axis (as might often be expected for a foreshortened disk). Of these two, one (Q1623-BX543) has a close ( $\sim 7$  kpc) companion which does not partake in the same pattern of velocity shear. A model for the single remaining galaxy, DSF2237a-C2, which is isolated and has a significant kinematic gradient aligned with its morphological major axis has been presented by Law et al. (2007a).

Absent such models, the best kinematic statistic available is the observed ratio  $v_{\text{shear}}/\sigma_{\text{mean}}$ , values of which range from 0.2 to 0.7 with a typical uncertainty of  $\sim 0.2$  (Table 5). While we have attempted to maximize the value of  $v_{\text{shear}}/\sigma_{\text{mean}}$  by appropriate choice of the position angle for our pseudo-slit, and by using the smaller of our two estimates of  $\sigma$ , the meaning of any particular value must be considered with regard to several important factors.

1. The observed velocity curves will be foreshortened by a factor of  $\sin i$ . On average this will introduce a correction factor of  $\pi/4$  (see the Appendix).
2. The OSIRIS data are relatively shallow and probe radii  $\lesssim 2$  kpc. If the velocity curve rises at larger radii, our observations will underestimate the true circular velocity of the system.

3. Unresolved kinematic structure smeared by the observational beam will decrease the observed velocity gradient and inflate the central velocity dispersion to which the flux-weighted  $\sigma_{\text{mean}}$  is most sensitive. In the case of a rotating disk model this effect will be particularly pronounced at small radii where the velocity gradient is steepest.

All of these effects will systematically produce values of  $v_{\text{shear}}/\sigma_{\text{mean}}$  lower than  $v_{\text{disk}}/\sigma_{\text{int}}$ , although the magnitude of these effects is difficult to quantify as they depend strongly upon the (unknown) intrinsic kinematic structure of the galaxies. Rotating disk models may expect correction factors  $\sim 2-4$  (the disk model for DSF2237a-C2 developed by Law et al. 2007a, for example, had a correction factor of  $\sim 2$ ), depending on the size of the observational PSF and the precise distribution of flux with respect to the underlying rotation field. Even allowing for an extreme correction factor of  $\sim 5$ , the observed range  $v_{\text{shear}}/\sigma_{\text{mean}} = 0.2-0.7$  is significantly lower than the typical values ( $v_{\text{disk}}/\sigma_{\text{int}} \sim 10-20$ , i.e.,  $v_{\text{shear}}/\sigma_{\text{mean}} \sim 2-4$ ) appropriate to disk galaxies today (e.g., Dib et al. 2006), in agreement with the general conclusion that these galaxies must be considerably thicker than traditional disk galaxies in the local universe (see also discussion by Förster Schreiber et al. 2006; Genzel et al. 2006, 2008; Law et al. 2007a).

Such corrections to the observational data may not obviously be desirable however for galaxies which are not well described by inclined disk models. In at least six of our 13 galaxies both the velocity and velocity dispersion are consistent with a constant value across multiple resolution elements. In the absence of coherent velocity structure, the high velocity dispersions observed for  $z \sim 2$  galaxies ( $\langle \sigma_{\text{mean}} \rangle = 78 \pm 17 \text{ km s}^{-1}$ ) cannot be explained by the convolution of such structure with the observa-

**Table 4**  
Stellar Population Parameters

Galaxy	$K_s^a$	$M_*^b$ ( $10^{10} M_\odot$ )	Age <sup>c</sup> (Myr)	SFR <sub>SED</sub> <sup>d</sup> ( $M_\odot \text{ yr}^{-1}$ )	SFR <sub>neb</sub> <sup>e</sup> ( $M_\odot \text{ yr}^{-1}$ )	SFR <sub>DKE</sub> <sup>f</sup> ( $M_\odot \text{ yr}^{-1}$ )	$E(B - V)^g$	$M_{\text{gas}}^h$ ( $10^{10} M_\odot$ )	$\mu^i$
Detections									
Q0449-BX93	20.51 [20.59]	0.9	203	47	13	...	0.135	...	...
Q1217-BX95	20.69 [20.79]	3.0	571	52	28	...	0.235	...	...
HDF-BX1564	19.62 [19.70]	2.9	571	53	31	34	0.205	3.6	0.55
Q1623-BX453	19.76 [20.00]	3.1	404	77	57	100	0.245	3.3	0.52
Q1623-BX502	22.04 [22.69]	0.3	203	15	24	79	0.130	3.5	0.92
Q1623-BX543	20.54 [20.66]	0.4	10	431	189	98	0.285	4.6	0.92
Q1700-BX490	19.99 [20.26]	0.4	10	441	154	160	0.280	5.6	0.93
Q1700-BX710	20.18 [20.23]	4.4	1278	34	15	59	0.195	2.5	0.36
Q1700-BX763	20.94 [20.98]	1.4	905	15	6	23	0.125	0.8	0.36
DSF2237a-C2	20.53 [20.71]	2.9	255	112	39	...	0.175	...	...
Q2343-BX418	21.88 [22.29]	0.1	102	11	17	32	0.030	1.4	0.93
Q2343-BX513	20.10 [20.16]	7.8	3000	26	13	44	0.155	1.8	0.19
Q2343-BX660	20.98 [21.21]	0.8	1609	5	19	30	0.005	1.8	0.69
Nondetections									
Q0100-BX210	...	0.8	102	74	...	...	0.215	...	...
HDF-BX1311	20.48	0.9	255	35	...	48	0.110	2.3	0.72
HDF-BX1439	19.72	4.6	2200	21	...	48	0.175	3.7	0.45
Q1623-BX455	21.56	0.8	45	175	...	169	0.370	5.4	0.87
Q1623-BX663 <sup>j</sup>	19.92	13.2	2000	21	...	50	0.135	2.7	0.17
Q1700-BX563	...	3.3	641	51	...	...	0.220	...	...
Q1700-BX691	20.68	6.0	2750	22	...	36	0.285	2.1	0.26
Q2206-BX102	...	11.8	2750	43	...	...	0.335	...	...
Q2343-BX389	20.18	7.2	2750	26	...	80	0.265	4.7	0.39
Q2343-BX442	19.85	11.8	2750	43	...	44	0.285	3.2	0.21
Q2343-BX587	20.12	3.3	719	46	...	32	0.175	2.1	0.39

**Notes.**

<sup>a</sup> Observed Vega magnitude, values in parentheses are corrected for line emission (where observed).

<sup>b</sup> Typical uncertainty  $\langle \sigma_{M_*} / M_* \rangle = 0.4$ .

<sup>c</sup> Typical uncertainty  $\langle \sigma_{\text{Age}} / \text{Age} \rangle = 0.5$ .

<sup>d</sup> SFR derived from stellar population model. Typical uncertainty  $\langle \sigma_{\text{SFR}} / \text{SFR} \rangle = 0.6$ .

<sup>e</sup> Extinction-corrected nebular SFR. Values for Q1623-BX543 extrapolated from [O III].

<sup>f</sup> Nebular SFR estimate from long-slit observations by Erb et al. (2006b), corrected for extinction and slit losses.

<sup>g</sup> Typical uncertainty  $\langle \sigma_{E(B-V)} / E(B-V) \rangle = 0.7$ .

<sup>h</sup> Gas masses taken from Erb et al. (2006c).

<sup>i</sup> Gas fraction.

<sup>j</sup> AGN.

tional PSF<sup>12</sup> (as, for instance, in the  $z \sim 1.6$  sample of Wright et al. 2009), and instead indicate that both the high velocity dispersion and low bulk motions about a preferred kinematic axis may be intrinsic properties of the ionized gas.

## 4. NOTES ON INDIVIDUAL GALAXIES

### 4.1. Q0449-BX93

This intermediate-mass galaxy ( $M_* = 0.9 \times 10^{10} M_\odot$ ) is dominated by a single emission component at the systemic redshift with a faint secondary component offset by  $\sim 150 \text{ km s}^{-1}$  located  $\sim 1 \text{ kpc}$  to the northeast. This faint secondary feature may represent a kinematically distinct star-forming region or a small galaxy in the process of merging with the brighter system (see discussion by Law et al. 2007a). Weak [N II] emission (both  $\lambda 6549$  and  $\lambda 6585$  lines are detected with similar significance) is roughly concentric with the H $\alpha$  emission and implies a metallicity  $12 + \log(\text{O}/\text{H}) = 8.37 \pm 0.09$  (approximately half-

solar). There is no evidence for significant bulk motions with  $v_{\text{shear}}/\sigma_{\text{mean}} = 0.2 \pm 0.2$ .

### 4.2. Q1217-BX95

This galaxy is qualitatively similar to Q0449-BX93, and is well detected but compact (only slightly larger than the observational PSF) with no evidence of extended structure despite its moderate stellar mass ( $3 \times 10^{10} M_\odot$ ). There is no obvious velocity structure within this source.

### 4.3. HDF-BX1564

HDF-BX1564 is among the least well detected of our galaxies, and required heavy spatial and spectral smoothing of the composite data cube in order to successfully discern emission features. This extensive processing has the unfortunate consequence of increasing our effective PSF to  $\sim 0''.3$ , comparable in size to the two primary emission regions (northwest (NW) and southeast (SE)) comprising the source. These two features are separated by  $v_{2c} \sim 171 \text{ km s}^{-1}$  and  $d_{2c} = 7 \text{ kpc}$ . While a third component is apparent in Figure 2, based on analysis of typical noise patterns within the composite data cube we believe that

<sup>12</sup> Numerical modeling suggests that beam smearing can account for at most a few percent of the observed  $\langle \sigma_{\text{mean}} \rangle$ .

**Table 5**  
Kinematic Properties

Galaxy	$\sigma_{\text{mean}}^{\text{a}}$ ( $\text{km s}^{-1}$ )	$\sigma_{\text{net}}^{\text{b}}$ ( $\text{km s}^{-1}$ )	$v_{\text{shear}}^{\text{c}}$ ( $\text{km s}^{-1}$ )	$v_{2c}^{\text{d}}$ ( $\text{km s}^{-1}$ )	$\Delta v_{(\text{ISM}-\text{neb})}^{\text{e}}$ ( $\text{km s}^{-1}$ )	P.A. <sup>f</sup> ( $^{\circ}$ )	$v_{\text{shear}}/\sigma_{\text{mean}}$	$M_{\text{dyn}}^{\text{g}}$ ( $10^{10} M_{\odot}$ )
Q0449-BX93	$56 \pm 20$	$71 \pm 5$	$13 \pm 8$	...	-270	330	$0.2 \pm 0.2$	0.5
Q1217-BX95	$69 \pm 23$	$61 \pm 5$	$12 \pm 13$	...	-298	110	$0.2 \pm 0.2$	0.3
HDF-BX1564	$60 \pm 13$ (NW) $86 \pm 8$ (SE)	$103 \pm 14$	$12 \pm 12$ (NW) $5 \pm 12$ (SE)	171	-447	325 (NW) 325 (SE)	$0.2 \pm 0.2$ (NW) $0.1 \pm 0.1$ (SE)	0.5 (NW) $\leq 0.9$ (NW)
Q1623-BX453	$78 \pm 23$	$94 \pm 5$	$29 \pm 10$	...	-849	45	$0.4 \pm 0.2$	1.0
Q1623-BX502	$67 \pm 20$	$68 \pm 3$	$35 \pm 11$	...	-67	30	$0.5 \pm 0.3$	0.7
Q1623-BX543	$139 \pm 32$ (N) $60 \pm 10$ (S)	$153 \pm 7$	$39 \pm 4$ (N) $22 \pm 9$ (S)	125	-94	315 (N) 225 (S)	$0.3 \pm 0.1$ (N) $0.4 \pm 0.2$ (S)	2.5 (N) 0.3 (S)
Q1700-BX490	$89 \pm 25$ (W) $65 \pm 29$ (E)	$122 \pm 6$	$50 \pm 10$ (W) $22 \pm 9$ (E)	109	106	200 (W) 270 (E)	$0.6 \pm 0.2$ (W) $0.5 \pm 0.3$ (E)	1.5 (W) 0.3 (E)
Q1700-BX710	$68 \pm 25$	$67 \pm 7$	$15 \pm 16$	...	118	0	$0.2 \pm 0.3$	0.6
Q1700-BX763	$50 \pm 14$	$53 \pm 5$	$14 \pm 16$	...	-264	320	$0.3 \pm 0.3$	0.3
DSF2237a-C2	$89 \pm 20$	$99 \pm 10$	$51 \pm 14$	...	125	220	$0.6 \pm 0.2$	0.8
Q2343-BX418	$61 \pm 17$	$70 \pm 5$	$23 \pm 12$	...	-209	70	$0.4 \pm 0.2$	0.3
Q2343-BX513	$100 \pm 25$	$102 \pm 6$	$65 \pm 16$	...	-19	180	$0.7 \pm 0.2$	1.6
Q2343-BX660	$71 \pm 16$	$73 \pm$	$40 \pm 9$	...	-274	45	$0.6 \pm 0.2$	0.9

**Notes.**

<sup>a</sup> Flux-weighted mean and standard deviation of velocity dispersions in individual spaxels in the OSIRIS map.

<sup>b</sup> Velocity dispersion of the spatially collapsed object spectrum. Uncertainty quoted is based on Monte Carlo analysis of synthetic spectra.

<sup>c</sup> Shear velocity  $v_{\text{shear}} = \frac{1}{2}(v_{\text{max}} - v_{\text{min}})$ .

<sup>d</sup> Velocity difference between two discrete components.

<sup>e</sup> Kinematic offset between ISM absorption line redshift and nebular emission-line redshift.

<sup>f</sup> Position angle of steepest velocity gradient.

<sup>g</sup> Single-component dynamical mass within the radius probed by nebular emission.

this feature is probably not real. Supporting this explanation is the rest-UV morphology, which we show for comparison in Figure 3. Both the NW and SE features have counterparts in the ACS imaging data, while the questionable northeastern feature does not. The *HST*-ACS imaging data also suggest faint diffuse emission in the field of view, particularly in the form of spurs reaching between the bright knots. Given that the bright knots themselves are only barely detected (at an S/N of  $\sim 5$ ) in the heavily smoothed OSIRIS data, it is not surprising that we do not detect these spurs, even if they have  $\text{H}\alpha$  counterparts.

The local velocity dispersions of the NW and SE features are  $60 \pm 13$  and  $86 \pm 8 \text{ km s}^{-1}$ , respectively, consistent with the typical values observed for the rest of the galaxy sample, while their effective PSF-corrected radii (Section 3.1) are 1.3 and 0.1 kpc (i.e., the SE feature is consistent with a point source given the size of the PSF). The respective dynamical masses of the two components are 0.5 and  $0.1 \times 10^{10} M_{\odot}$ . Given the poorly resolved nature of the SE component however, the radius of this object is particularly ill-defined and given the similar values of  $\sigma_{\text{mean}}$  for the two components they may be of approximately equal mass.

The multiple components and low surface brightness features in the UV morphology may indicate that HDF-BX1564 is an ( $\sim$ equal mass) major merger (although see discussion by Law et al. 2007b). In this case, additional insight may be gained from Keck/NIRSPEC long-slit spectroscopy obtained in 2004 June (see Erb et al. 2006b) with a  $0''.76$  wide slit aligned along the axis between the two major components to within  $5^{\circ}$ . As illustrated in Figure 6, both primary components are well detected in the spectrum with similar kinematic and spatial separation as in the OSIRIS data. In this considerably deeper observation there is evidence for nebular emission extending between the two components, the SE feature has a spatial FWHM of  $1''.1$  and reaches all the way to the NW component, whose  $0''.6$  FWHM

is more closely matched to the PSF of these seeing-limited data. Notably, there is no gradual shift in wavelength along the axis connecting the two, but instead a sharp transition upon reaching the NW feature, suggesting that the emitting material between the two components does not partake in a smoothly varying velocity curve and bolstering the case for a major merger interpretation of this galaxy.

Intriguingly, there is faint detection of [N II] emission ( $12+\log(\text{O}/\text{H}) = 8.67 \pm 0.04$ ) in the OSIRIS data centered on neither of the two primary  $\text{H}\alpha$  emitting regions, but on a region of space between them corresponding to a faint spur in the rest-UV morphology (Figure 3). This may suggest the presence of an obscured active galactic nucleus (AGN) at the dynamical center of this system (although neither the rest-UV spectrum nor the SED shows evidence for an active nucleus), while the UV and nebular line emission are dominated by off-center regions of relatively unobscured star formation. Alternatively, this could be evidence for diffuse shocked gas, or low ionization parameter gas as discussed by Martin (1997). Given the low S/N of our data, however, it is not possible to conclusively explain the observational complexities of this system.

#### 4.4. Q1623-BX453

As discussed in Law et al. (2007a) this galaxy is one of the best examples of the “typical” kinematics observed in our sample, with spatially well-resolved nebular emission exhibiting a negligible velocity differential across the majority of the galaxy and kinematically dominated by a high local velocity dispersion  $\sigma_{\text{mean}} = 78 \pm 23 \text{ km s}^{-1}$ . The  $v_{\text{shear}}/\sigma_{\text{mean}}$  value calculated for this galaxy is dominated by a region of high relative velocity at the northeastern end of the galaxy. This region is detected with low confidence however (S/N  $\sim 4$ ) and represents an abrupt kinematic discontinuity rather than an extended gradient.

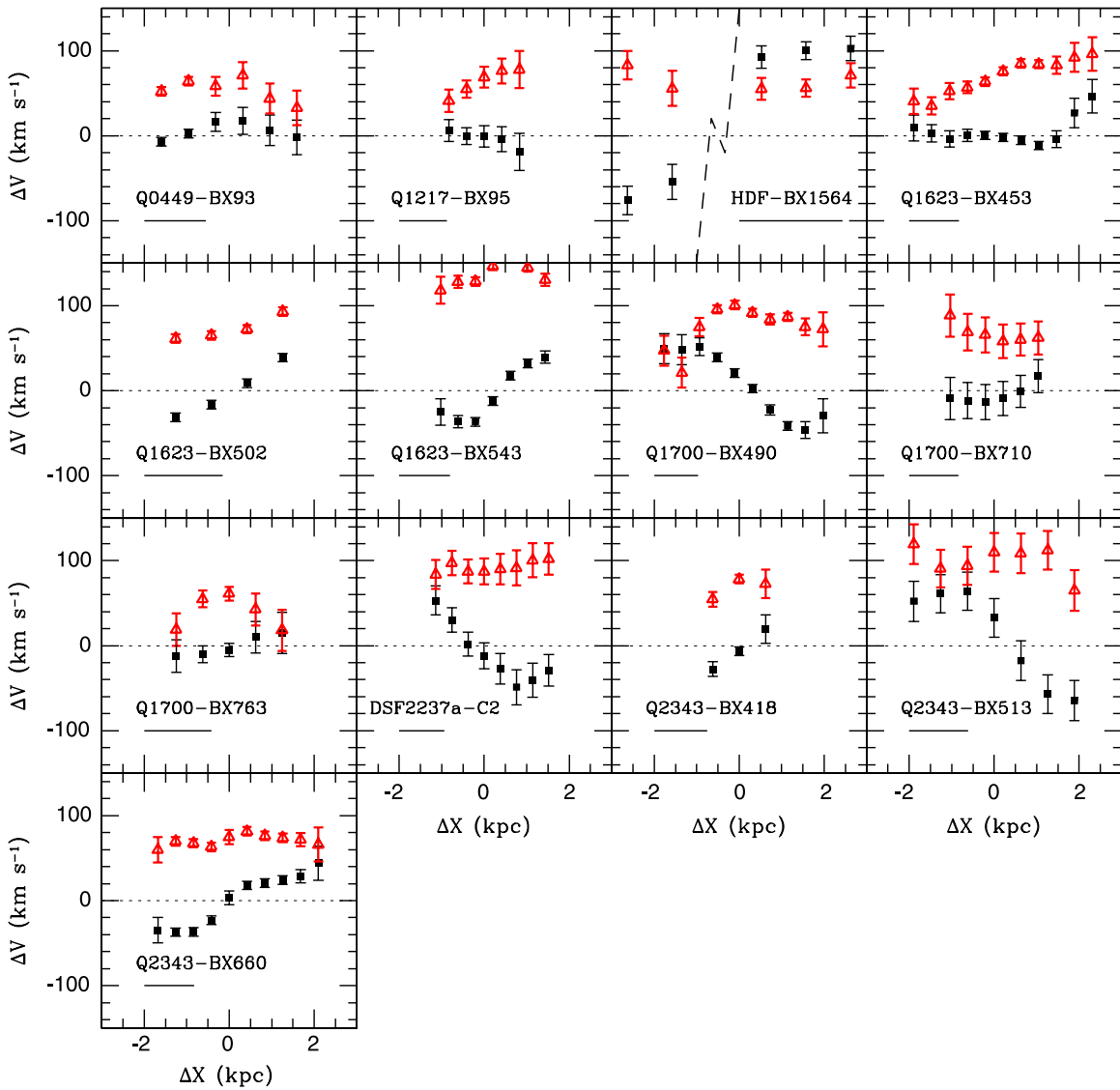


**Figure 5.** Relative velocity (black filled squares) and velocity dispersion (red open triangles) curves along the kinematic major axis for each galaxy (see Figure 2 for orientation). The solid line in each panel represents the FWHM of each observation, the sampling scale in each panel corresponds to half of this value to minimize spatial correlation between individual points. Error bars represent uncertainties derived from numerical Monte Carlo modeling. Note that the plot for HDF-BX1564 is discontinuous and omits a 4 kpc region of blank sky between the two components in order to fit both into the same display area as the other galaxies.

(A color version of this figure is available in the online journal.)

Q1623-BX453 is inferred to have a large amount of cold gas, a sizeable stellar mass ( $\sim 3 \times 10^{10} M_{\odot}$ ), high metallicity ( $12 + \log(\text{O}/\text{H}) = 8.67 \pm 0.02$ ), and a high SFR surface density with a correspondingly large outflow velocity of  $\sim 900 \text{ km s}^{-1}$  as traced by rest-UV spectroscopy of interstellar absorption lines. Given the large quantity of cold gas in this galaxy, it is particularly intriguing that there is no evidence for the rotational structure in which such gas is traditionally supposed to reside.

#### 4.5. Q1623-BX502

Q1623-BX502 is one of the lowest stellar mass objects observed with OSIRIS ( $M_{*} = 3 \times 10^9 M_{\odot}$ ) and is the only galaxy to be successfully detected under poor observing conditions with high humidity and V-band seeing  $\gtrsim 1''$ . These suboptimal observing conditions are reflected in the relatively broad PSF (220 mas) compared to the other galaxies in Figure 2. In addition, Q1623-BX502 was one of two galaxies which required correction for a spatially distorted PSF as described

in Section 2.3. While there is evidence for resolved velocity structure with peak amplitude of  $\sim 50 \text{ km s}^{-1}$ , this shear is not aligned with any obvious morphological major axis. A similar result was derived from the SINFONI observations of this galaxy by Förster Schreiber et al. (2006).

#### 4.6. Q1623-BX543

This galaxy consists of two spatially distinct components separated by  $v_{2c} = 125 \text{ km s}^{-1}$  and  $d_{2c} = 6.7 \text{ kpc}$  ( $0''.8$ ) in projection (with one almost due north of the other). Both components are present in our deep ground-based  $\mathcal{R}$ -band imaging, which shows a slight elongation along the north–south axis, indicating that both components correspond to rest-UV continuum emission regions. Given the typical  $\sim 1''$  PSF of this rest-UV imaging data however it is not possible to determine whether the continuum image consists of a single elongated feature or two separate features similar to those shown in Figure 2.



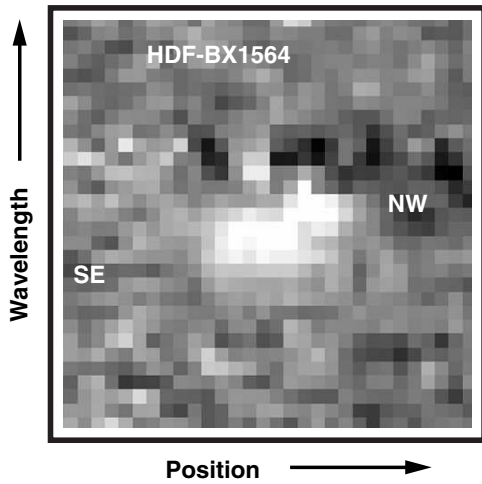


**Figure 6.** Two-dimensional NIRSPEC long-slit spectrum of HDF-BX1564. Each pixel corresponds to  $0''.143$  along the spatial and  $4.2 \text{ \AA}$  along the spectral axes. Note the abrupt wavelength transition between SE and NW components.

While not apparent in Figure 2 due to the limitations imposed by the dynamic range of the velocity scale, there is velocity structure within the northernmost (N) component. In Figure 7, we plot an expanded view of each of the components which better shows this structure. While the general trend is along a roughly NW–SE axis (see also Figure 5) there are appreciable deviations from a smooth trend along this axis. We note particularly that the relative velocity of the southern (S) component is strongly inconsistent with a smooth continuation of this velocity field (i.e., it would need to be *blueshifted* relative to systemic rather than redshifted). Given these discrepancies it is clearly impossible to fit both components of this system with a single simple kinematic model.

Perhaps the most likely scenario is that the primary (N) component is akin to the typical single galaxies observed in the rest of our sample, which in this case is experiencing a merger with the smaller S component. The northern and southern components have  $\sigma_{\text{mean}} = 139$  and  $60 \text{ km s}^{-1}$ , and effective radii  $r = 1.1$  and  $0.7 \text{ kpc}$ , respectively. Assuming that each component is relaxed and kinematically dominated by  $\sigma_{\text{mean}}$  we obtain (Equation (2)) estimates of the dynamical masses  $M_{\text{dyn}} \sim 2.5$  and  $0.3 \times 10^{10} M_{\odot}$ . If this system is a merger, these rough calculations suggest that the mass ratio of the merger is  $\sim 8/1$ .

While it is somewhat curious that the photometry of this source is (relatively) well fit by a simple stellar population

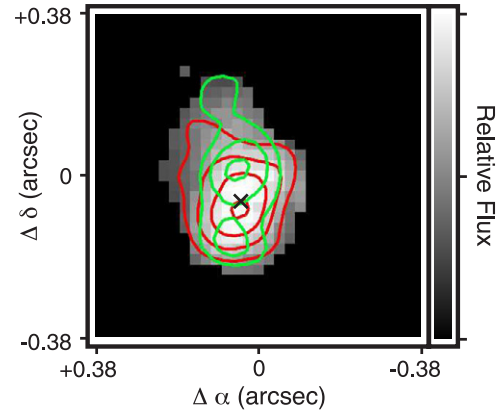


**Figure 8.** Flux map of Q2343-BX513 overlaid with contours showing the distribution of flux in the blue and red sides of  $H\alpha$  emission (the green and red contours, respectively). The wavelength difference between the two sets of contours is  $10 \text{ \AA}$ , or  $150 \text{ km s}^{-1}$  at the redshift of the galaxy. The black cross indicates the location of peak  $[N \text{ II}]$  emission.

model, such a mass ratio suggests that the larger of the two components may constitute the bulk of both the current and past star formation in the system. The total stellar mass of the system is quite small ( $4 \times 10^9 M_{\odot}$ ) with an extremely young stellar population as might be expected if rapid star formation<sup>13</sup> is occurring as a result of the rapid injection of large quantities of cold gas.

#### 4.7. Q1700-BX490

As in the case of Q1623-BX543, this galaxy has a complex, multiple-component structure. As demonstrated by Figure 3, the overall location and size of these two components is broadly consistent with *HST*-ACS rest-UV imaging. At the fainter surface brightness levels probed by *HST*-ACS both components are enclosed in a common envelope of flux, and it is probable that the discontinuous  $H\alpha$  morphology is simply a consequence of our limiting surface brightness sensitivity. Curiously, the western (W) component has a single well defined peak to the UV flux distribution located between the double peaks of nebular  $H\alpha$  emission (see the contours in Figure 3).

In the larger W component there is a smoothly varying velocity gradient along the northeast–southwest axis (i.e., not aligned

<sup>13</sup> The high SED-derived SFR given in Table 4 for Q1623-BX543 and Q1700-BX490 are likely significantly overestimated, and the 10 Myr ages highly uncertain due to difficulties fitting appropriate  $E(B - V)$  for these very young galaxies (see discussion in Reddy et al. 2006b).

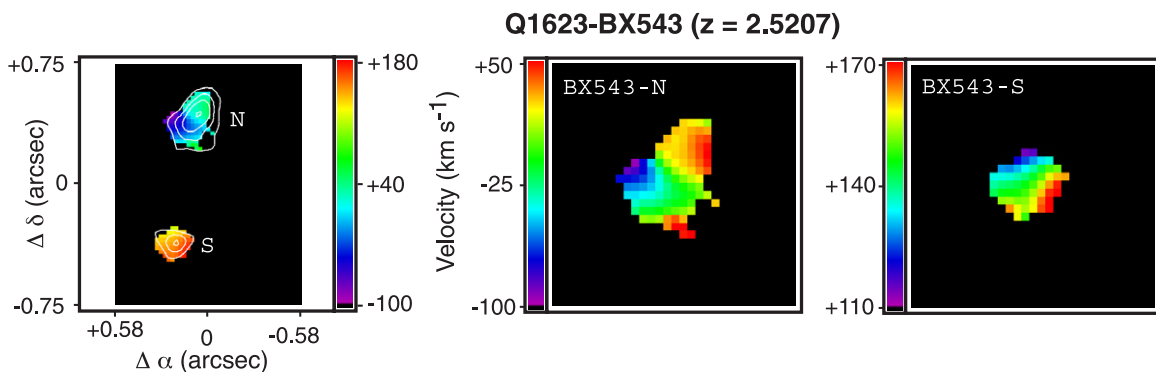


**Figure 7.** Velocity map of Q1623-BX543 (left panel, see also Figure 2) is expanded about each of the two components labeled north (“N”) and south (“S”). The color scale represents line-of-sight velocity relative to the systemic redshift in all three panels, the limits of this velocity scale vary as indicated to best illustrate the velocity features of each component.

with the east–west major axis of the *HST*-ACS morphology) from which emission-line flux appears to be concentrated in two closely separated knots. Rather than peaking in the center of the object as might be expected for a rotating gaseous disk (although see discussion by Wright et al. 2009), the velocity dispersion instead peaks in one of these two knots. While the smaller eastern (E) component is close to the main body in projection (3.4 kpc) and would likely appear to connect with the W component in deeper spectroscopic data, it does not partake in the velocity gradient defined by the W body. Rather, it has its own (albeit weak) velocity gradient aligned nearly perpendicular ( $\sim 70^\circ$ ) to that of the main body.

Paired with the additional faint structure evident in the *HST*-ACS image (note particularly another low surface brightness component southwest of the main body) one natural explanation for this galaxy may be that it represents a merger (mass ratio  $\sim 5/1$ ) with multiple sites of star formation. The broadband photometry is extremely well fit by a young (10 Myr) stellar population model with a small stellar mass ( $4 \times 10^9 M_\odot$ ) and a high current SFR. This galaxy is also likely quite metal-poor as [N II] is undetected, placing a limit  $12 + \log(\text{O}/\text{H}) \leq 8.26$  ( $\leq 2/5$  solar).

#### 4.8. Q1700-BX710

As for Q1623-BX453, this galaxy is relatively well-resolved with no strong evidence for spatially resolved velocity structure. While [N II] is detected in emission, it is weak ( $12 + \log(\text{O}/\text{H}) = 8.40 \pm 0.08$ ) and consistent with a point source roughly concentric with the  $\text{H}\alpha$  flux peak. There is a slightly redshifted extension of flux to the northwest of the galaxy core which has a lower velocity dispersion and is coincident with the low surface brightness emission tail seen in *HST*-ACS imaging data (Figure 3). We note that another galaxy (Q1700-BX711) is located  $\sim 5''$  (41 kpc) to the northwest of Q1700-BX710 (i.e., approximately along the direction of the “tail” indicated by the *HST*-ACS data) and at the same redshift to within  $10 \text{ km s}^{-1}$ . However, a long-slit NIRSPEC spectrum obtained along the line connecting the two galaxies shows no evidence for star formation occurring in the region between the two galaxies. If these galaxies are genuinely close in space as implied by their redshifts they may merge over the next few hundred Myr.

#### 4.9. Q1700-BX763

Q1700-BX763 has an apparent western spur to the  $\text{H}\alpha$  flux consistent with that observed in *HST*-ACS imaging data. While there is mild evidence for a velocity gradient along this spur the magnitude of this gradient is small and its significance low (Figure 5). As for Q1700-BX710, weak [N II] emission is detected (implying  $12 + \log(\text{O}/\text{H}) = 8.41 \pm 0.25$ ) that is consistent with a point source and is roughly (within  $\sim 0''.1$ ) concentric with the  $\text{H}\alpha$  emission peak.

#### 4.10. DSF2237a-C2

DSF2237a-C2 is located at a significantly higher redshift than any other galaxies in the target sample ( $z \sim 3.3$ ), and is drawn from the “LBG” galaxy catalog of Steidel et al. (2003). Given its high redshift, it is interesting that DSF2237a-C2 has some of the strongest velocity shear observed in our sample ( $v_{\text{shear}}/\sigma_{\text{mean}} = 0.6 \pm 0.2$ ) and is the only isolated case where this shear is consistent with rotation and unambiguously aligned with the morphological major axis. Nonetheless, the local velocity dispersion of DSF2237a-C2 is comparable to that

of the rest of the galaxy sample with  $\sigma_{\text{mean}} = 89 \pm 20 \text{ km s}^{-1}$ . We note that this galaxy was discussed previously by Law et al. (2007a), although various estimate of the kinematics and flux parameters have been updated here for consistency with our new calibration routines.<sup>14</sup>

#### 4.11. Q2343-BX418

As for Q1217-BX95, Q2343-BX418 is well detected in the composite OSIRIS data cube but is spatially compact with a slight elongation along the north–south axis. While there is some evidence for coherent velocity structure aligned with the morphological minor axis, the magnitude of this shear is significantly smaller than the local velocity dispersion. We note additionally that this is our lowest mass galaxy with  $M_* = 1 \times 10^9 M_\odot$ , a similarly small dynamical mass estimate  $M_{\text{dyn}} = 3 \times 10^9 M_\odot$  and very little dust ( $E(B - V) = 0.03$ ). With so little extinction, Q2343-BX418 is also a strong Ly $\alpha$  emitting source (see M. Pettini et al. 2009, in preparation).

#### 4.12. Q2343-BX513

Q2343-BX513 is elongated along the north–south axis and exhibits a complex velocity structure composed of multiple spatially superimposed components. At first glance the one-dimensional velocity curve in Figure 5 (with  $v_{\text{shear}}/\sigma_{\text{mean}} = 0.7 \pm 0.2$ ) gives an indication of smooth resolved velocity shear in this source, but the two-dimensional velocity map (see Figure 2) is inconsistent with a simple rotational model. Following the velocity pattern from north to south, we find that the northernmost region is blueshifted by  $-80 \text{ km s}^{-1}$  (relative to the systemic redshift); moving south we reach a maximum redshift of  $v = +50 \text{ km s}^{-1}$  near the flux peak, but then the velocity falls off again to lower values, down to  $v \simeq 0 \text{ km s}^{-1}$  at the southern edge of the galaxy. Indeed, if we consider the spatial distribution of the red and blue sides of the  $\text{H}\alpha$  emission individually we note that while the redder component is well centered, the blue edge of  $\text{H}\alpha$  emission is dominated by two distinct emission regions located directly north and south of the center (Figure 8). The total  $\text{H}\alpha$  flux of Q2343-BX513 is dominated by the centrally concentrated redshifted component.

This double-component morphology helps to explain the previous long-slit observations of Erb et al. (2006c) who found two slightly different redshifts for the system with different  $\sigma$  when the galaxy was observed at two different position angles. Notably, the galaxy also has a highly unusual double-featured UV spectrum with Ly $\alpha$  emission at redshifts  $z = 2.106$  and  $2.114$  (i.e., offset by  $770 \text{ km s}^{-1}$ ) and possible doubles of the strongest interstellar absorption lines, such as Si II  $\lambda 1260$ , O I + S II  $\lambda 1302$ , and C II  $\lambda 1334$ . This spectrum is additionally confused by the presence of absorption lines arising in an intervening system Q2343-MD80 ( $z = 2.014$ ) located a few arcseconds away. [N II]  $\lambda 6583$  is detected with a strength relative to  $\text{H}\alpha$  which implies  $12 + \log(\text{O}/\text{H}) = 8.63 \pm 0.03$ , close to the solar oxygen abundance, and is roughly concentric with the redder  $\text{H}\alpha$  component with a similar north–south elongation. There is a significant velocity gradient in the [N II] emission with an end-to-end velocity differential of  $\sim 110 \text{ km s}^{-1}$ .

<sup>14</sup> In particular, the value of  $L_{[\text{O III}]}$  in Table 3 of Law et al. (2007a) was incorrectly given as  $2.2 \times 10^{42} \text{ erg s}^{-1}$ , while it should instead have been given as  $22 \times 10^{42} \text{ erg s}^{-1}$ . The revised number is consistent with the estimate of  $16.8 \times 10^{42} \text{ erg s}^{-1}$  derived using our new flux calibration routine.

We note that this galaxy is the oldest in the OSIRIS sample (among both detected and undetected targets) with an estimated stellar population age of  $\sim 3$  Gyr and a large stellar mass  $M_* = 7.8 \times 10^{10} M_\odot$ . One possibility, therefore may be that the redshifted component (with associated [N II] emission and the larger velocity dispersion) is the massive “mature” galaxy which contains the majority of the evolved stellar population and has an appreciable velocity gradient (as expected for such a massive galaxy; see discussion in Section 5). Behind this component may be a smaller (infalling) system which is partially obscured by the central core of the foreground galaxy, causing the apparent two-component morphology. While it is beyond the scope of the present work to verify this hypothesis (and indeed, the two components may simply be unrelated juxtapositions in redshift space), we may certainly conclude that this system is particularly complex.

#### 4.13. Q2343-BX660

The  $H\alpha$  morphology of Q2343-BX660 is composed of two spatially distinct peaks (which are more apparent in the three-dimensional data cube than in the collapsed  $H\alpha$  map) which blend together at low surface brightness to form a contiguous system. While there is a strong velocity differential across the combined system, the line-of-sight velocity remains relatively constant across each of these two clumps and changes rapidly in the region between the two ( $\sim 80 \text{ km s}^{-1}$  over less than  $0''.1$ ). While turnovers in the velocity profile are naturally found in rotating systems beyond a certain radius, it is suspicious that the entire velocity gradient of this galaxy is contained within a single angular resolution element (corresponding to a radius of  $\sim 400 \text{ pc}$ ).

Instead, this figure is reminiscent of Figure 8 in Law et al. (2006), whose panel (d) shows the nearly identical velocity map expected for a two-clump velocity model in which the apparent scale of the “turnover” is determined by the observational PSF blurring together emission from the two regions. Indeed, Nesvadba et al. (2008; see also Wright et al. 2009) recently presented observations of a galaxy at  $z \sim 3$  (Q0347-383 C5) which showed a very similar velocity structure, transitioning rapidly from a plateau of  $\sim 60 \text{ km s}^{-1}$  to  $\sim -80 \text{ km s}^{-1}$  within a negligible physical distance, leading the authors to favor a merger interpretation for the galaxy. Similarly, we conclude that the kinematics of Q2343-BX660 are more consistent with merging compact galaxies than with underlying rotation in a single relaxed system. Given the relative constancy of  $\sigma$  across the galaxy we surmise that in such an event the mass ratio should be  $\lesssim 3/1$ , with a total stellar mass of  $\sim 10^{10} M_\odot$ .

## 5. DISCUSSION

### 5.1. Selection Effects

As outlined in Section 2.1, targets were selected from the rest-UV galaxy sample for a wide variety of reasons (high/low stellar mass, extended/compact morphology, presence/absence of kinematic shear in long-slit spectra, etc.) subject to the general criterion that we believed the galaxy would be detected on the basis of previous long-slit observations (Erb et al. 2006b) or narrowband  $H\alpha$  imaging. While our original choice of targets attempted to include a wide range of galaxy properties, it is still difficult to know how representative our results are of the general population of star-forming galaxies at  $z = 2-3$ , given the large fraction of targets which were undetected

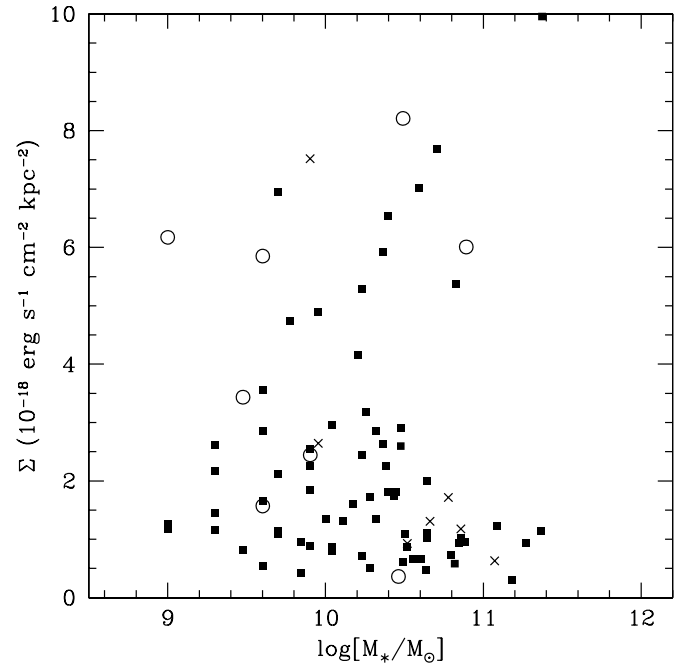


**Figure 9.** Mean  $H\alpha$  surface brightness as a function of stellar mass for the Erb et al. (2006c) long-slit survey of galaxy kinematics. Data are plotted for all galaxies in the Erb et al. (2006c) survey in the redshift range  $z = 1.9-2.5$  which have well defined values of both the  $H\alpha$  flux and galaxy size. The open circles represent galaxies which have been successfully observed with OSIRIS, crosses galaxies which were either undetected or poorly detected with OSIRIS, and filled squares galaxies not observed with OSIRIS.

or poorly detected (11 out of 24) despite extensive observational efforts (see Table 1). This bias is difficult to quantify since the probability of detecting a given galaxy is a strong function of observing conditions; 11 of the 16 unsuccessful observations (some of which represent multiple attempts to observe the same galaxy) listed in Table 1 were performed under suboptimal conditions typically characterized by poor seeing  $\gtrsim 1''$  (resulting in poorer AO correction), high humidity (exacerbating telluric absorption), and/or attenuation by cirrus ( $\gtrsim 1 \text{ mag}$ ). In contrast, only one of our successfully detected galaxies (Q1623-BX502) was observed under similarly poor conditions.

The likelihood of detection was probably also governed by the  $H\alpha$  surface brightness of the target galaxies. In Figure 9, we plot the surface brightness  $\Sigma = F_{H\alpha}/r_{H\alpha}^2$  of galaxies targeted by the Erb et al. (2006c; based on values given in their Table 4) long-slit spectroscopic survey, indicating galaxies which were detected/undetected in the OSIRIS observations. While the results naturally will be quite inhomogenous given the widely varying weather conditions and exposure times of the OSIRIS observations we note that the mean surface brightness of galaxies in the NIRSPEC survey which were successfully detected with OSIRIS is  $4.3 \times 10^{-18} \text{ erg s}^{-1} \text{ cm}^{-2} \text{ kpc}^{-2}$ , compared to  $2.3 \times 10^{-18} \text{ erg s}^{-1} \text{ cm}^{-2} \text{ kpc}^{-2}$  for galaxies either undetected or poorly detected with OSIRIS, and a mean/median of  $2.6/1.7 \times 10^{-18} \text{ erg s}^{-1} \text{ cm}^{-2} \text{ kpc}^{-2}$ , respectively for the entire NIRSPEC sample. Clearly, we are observing a population of galaxies with somewhat higher than average SFR surface density.

Such a surface brightness limit will also bias our observations toward high surface brightness regions within a given galaxy. Indeed, evidence suggests that at least some of the observations may genuinely be missing some flux from fainter surface

brightness regions. First, the integrated  $H\alpha$  fluxes are about half the aperture-corrected values determined from long-slit spectroscopy by Erb et al. (2006b), although in some cases this may also indicate that the aperture correction adopted for the long-slit data was overestimated. Similarly, galaxy sizes estimated from the long-slit program tend to be somewhat larger (although considerably less certain given the seeing-limited PSF) than those from OSIRIS. Additionally, the dynamical mass estimates are considerably less than the total of the stellar + gas masses, as might be expected if the radius of the system is underestimated in Equation (2) (or the stellar and/or gas masses are distributed over a larger volume than the ionized gas traced by OSIRIS).

In some cases (e.g., DSF2237a-C2), the kinematics suggest that the rotation curve may continue to rise at larger radii, meaning that deeper spectroscopy could result in larger values for  $v_{\text{shear}}$ . This is unlikely to be the case in general, however, since at least six of the 13 galaxies are consistent with a velocity gradient of  $\frac{dv}{dx} = 0 \text{ km s}^{-1} \text{ kpc}^{-1}$ . Indeed, deeper imaging of one galaxy (Q1623-BX502) with VLT/SINFONI (Förster Schreiber et al. 2006) showed no evidence for significant flux or velocity shear beyond that seen with OSIRIS.

Figure 9 also suggests that we are more likely to detect younger galaxies than older galaxies with a larger established stellar mass. The 13 galaxies detected with OSIRIS have a mean assembled stellar mass  $\langle \log(M_*/M_\odot) \rangle = 10.1$ , compared to the mean  $\langle \log(M_*/M_\odot) \rangle = 10.6$  (i.e., three times more massive) of the 11 galaxies which were undetected (or only poorly detected) in the OSIRIS data. Thus, while our sample may be representative of typical-mass galaxies in the star-forming population (the full sample of 818 optically selected galaxies at redshifts  $1.8 < z < 2.6$  with stellar mass information in our various survey fields has a mean stellar mass  $\langle \log(M_*/M_\odot) \rangle = 10.07$ ; Figure 10; see also Reddy et al. 2006a), the observations presented here are not particularly sensitive to the high-mass end of the star-forming galaxy distribution. We note for completeness however that all of these masses are high relative to the total galaxy population (i.e., including both UV-bright and faint galaxies). Integrating the stellar mass function given by Reddy & Steidel (2009) suggests that while galaxies in the stellar mass range probed by OSIRIS (i.e.,  $(0.1-7.8) \times 10^{10} M_\odot$ ) constitute  $\sim 66\%$  of the total space density of galaxies at  $z \sim 2$ , 90% of the total population have masses smaller than the average of the OSIRIS sample.

### 5.2. Expanding the Sample

In order to construct a more complete picture of the overall  $z \sim 2$  galaxy population we therefore combine our results with those of similar studies recently undertaken by a variety of authors. The largest sample of IFS observations of galaxies at redshift  $z \sim 2$  to date is the ‘‘SINS’’ survey using SINFONI on the VLT, the results of which have been presented by Förster Schreiber et al. (2006); Genzel et al. (2006); Bouché et al. (2007); and more recently Shapiro et al. (2008) and Genzel et al. (2008).<sup>15</sup> While all of the SINS galaxies (a few of which are in common with the present survey) exhibit comparably high velocity dispersions to the 13 OSIRIS galaxies reported here, many of them also show ordered velocity shear  $\gtrsim 100 \text{ km s}^{-1}$  to which Genzel and collaborators (see particularly Shapiro et al. 2008) have been relatively successful in fitting turbulent disk models.

In part, the different prevalence of shear between the SINS and OSIRIS surveys is a consequence of their sensitivity. Due to a combination of optical design differences and a larger ( $0''.1$ ) spaxel scale SINFONI is roughly twice as sensitive as OSIRIS and therefore able to probe fainter surface brightness features to larger radii. Combined with longer integration times (18,000 s vs. 8100 s in the case of Q2343-BX389, for example), SINFONI is capable of detecting large-scale velocity gradients in lower surface brightness galaxies undetectable with OSIRIS. In contrast, the image quality of the OSIRIS data is generally superior, with LGSAO image correction for all of the target galaxies and a typical PSF  $\sim 100 \text{ mas}$ , compared to the large fraction of the SINS sample (13 of the 14 galaxies discussed by Förster Schreiber et al. 2006) which were obtained in a seeing-limited mode with a PSF  $\sim 500 \text{ mas}$  (with some notable exceptions; e.g., Genzel et al. 2006). One simple explanation may therefore be that velocity shear is less noticeable in the inner few kpc of  $z \sim 2$  star-forming galaxies (where the OSIRIS survey is most sensitive) and only becomes significant relative to the line-of-sight velocity dispersion at larger radii and fainter surface brightnesses (where the SINS survey is most sensitive). Indeed, the maximum kinematic *slope* of DSF227a-C2 (the galaxy which presents the strongest case for resolved velocity shear in an inclined system for the OSIRIS sample)  $\frac{dv}{dx} \sim 35 \text{ km s}^{-1} \text{ kpc}^{-1}$  is comparable to that of the weakest rotator in the Genzel et al. (2008) sample (SSA22a-MD41), and if this slope extends to larger radii the two galaxies may also have comparable  $v_{\text{shear}}$  when observed to a similar limiting surface brightness.

In general, however, such a purely instrumental bias between the two surveys is an unsatisfactory explanation for the observed kinematic differences. While the upper end of the kinematic slopes observed with OSIRIS overlaps with that of the SINFONI ‘‘massive disk’’ population, the mean value for the 13 galaxies presented here ( $\langle \frac{dv}{dx} \rangle = 19 \text{ km s}^{-1} \text{ kpc}^{-1}$ ) is substantially less than the mean ( $\langle \frac{dv}{dx} \rangle = 47 \text{ km s}^{-1} \text{ kpc}^{-1}$ ) of the five galaxies discussed by Genzel et al. (2008). Indeed, six of the 13 galaxies observed with OSIRIS have  $\frac{dv}{dx}$  consistent with 0 to within observational uncertainty. In addition, both SINFONI and OSIRIS find similar kinematics in the few galaxies (e.g., Q1623-BX502) which were successfully observed by both surveys and do not indicate substantial shear in a low surface brightness component.

Most likely, the kinematics probed by the two surveys represent a continuum ranging from genuinely dispersion-dominated to rotationally supported systems. This range in kinematic properties is perhaps unsurprising in light of the relative physical properties of the galaxies included in the two samples. As discussed above, OSIRIS targets were drawn from the optically selected ‘‘BX’’ galaxy sample; the successful observations tend to have stellar masses in the less-massive to typical-mass range. In contrast, many of the SINS galaxies with significant velocity shear have inferred stellar masses that would place them in the top quartile of the general ‘‘BX’’ sample. Förster Schreiber et al. (2006) discuss a sample of 12 UV-selected galaxies (excluding Q1307-BM1163 due to its lower redshift, and Q1623-BX663 due to its subsequent identification as an AGN) with a similar range in  $M_*$  compared to the OSIRIS sample. The four galaxies in the sample with unambiguous velocity gradients with  $v_{\text{shear}} \gtrsim 100 \text{ km s}^{-1}$  (SSA22-MD41, Q2343-BX389, Q2343-BX610, and Q2346-BX482) have an average stellar mass  $\langle \log(M_*/M_\odot) \rangle = 10.99$ , eight times greater than the average of the rest-UV-selected

<sup>15</sup> We refer the reader also to Förster Schreiber et al. (2009), which first became available during the publication process of this paper.

population.<sup>16</sup> In their detailed discussion of disk kinematics, Shapiro et al. (2008) compare to a similarly high-mass subset of 11 galaxies chosen for their particularly high-quality data. The mean stellar mass of their five rest-UV-selected galaxies is  $(\log(M_*/M_\odot)) = 10.9$ , the remaining six are selected according to their rest-frame optical  $BzK$  color (e.g., Daddi et al. 2004). While there is a large amount of overlap between the BX and  $BzK$  samples, the particular  $BzK$  objects selected all have bright  $K$ -band magnitudes ( $K_s < 20.5$ ) whereas the BX objects (selected without regard to  $K$  magnitude) extend considerably fainter, to  $K_s \sim 22$  (see discussion by Reddy et al. 2006b). The  $BzK$  sample also tend to be slightly less strongly nucleated with fewer spatial irregularities (see discussion by Law et al. 2007b), consistent with the interpretation that they might more accurately be described as evolved stellar “disks” than the BX sample. The Bouché et al. (2007) sample in turn is roughly a superset of the Förster Schreiber et al. (2006) rest-UV-selected galaxies,  $K$ -bright rest-optically selected galaxies, and submillimeter galaxies (e.g., Chapman et al. 2005). In turn, Genzel et al. (2008) focus on five primary galaxies (four previously discussed by Förster Schreiber et al. 2006 and one additional galaxy BzK6004) with a mean stellar mass  $(\log(M_*/M_\odot)) = 11.0$ , 8.5 times larger than the mean of the rest-UV-selected population, and more massive than >99% of the overall  $z \sim 2$  galaxy population (based on the mass function of Reddy & Steidel 2009).

These data are summarized in Table 6 and Figure 10, which plots the maximum observed shear velocity of galaxies as a function of stellar mass. While there is considerable scatter in the diagram (unsurprisingly given that  $v_{\text{shear}}$  is not, and in most cases cannot, be corrected for inclination) we note that *all* galaxies with  $v_{\text{shear}}$  greater than the typical velocity dispersion have masses 2–20 times greater than the average for rest-UV-selected galaxies at these redshifts.

If velocity shear is indicative of systematic rotation, this suggests that stable rotation may be more prevalent (or at least more easily observed) among galaxies which have already accumulated a sizeable stellar population. It may be that the lowest mass galaxies tend to display negligible velocity shear and extremely high  $H\alpha$  surface brightness, while star formation in more massive galaxies with appreciable old stellar populations tends to trace the kinematics of any underlying disks with greater fidelity. While this trend might hold in a *statistical* sense, however, we stress that individual galaxies do not always fit this relation: one of our highest mass objects (Q2343-BX453) is perhaps the single best example of a galaxy without any resolved large-scale kinematic structure, while some low-mass objects (Q1700-BX490) show obvious structure. Indeed, the observation by Stark et al. (2008) of a gravitationally lensed galaxy offered an exceptionally fine-scale (resolution  $\sim 100$  pc) view of a low-mass galaxy whose stellar mass and velocity structure are remarkably similar to that of Q1700-BX490 (Table 6) with smoothly varying velocity shear.

### 5.3. Local Analogues and Galaxy–Galaxy Mergers

Recent studies of the clustering properties of  $z \sim 2$  star-forming galaxies in conjunction with large cosmological  $N$ -body simulations (e.g., Springel et al. 2005) have indicated (Conroy et al. 2008; Genel et al. 2008) that these galaxies

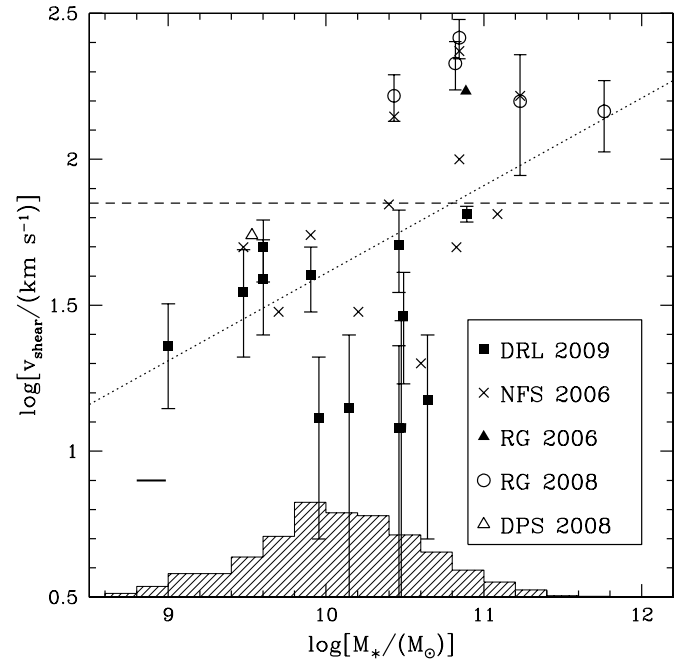


**Figure 10.** Logarithmic plot of stellar mass vs. maximum line-of-sight velocity shear for our 15 galaxies (DRL 2009) and galaxies discussed by Förster Schreiber et al. (2006; NFS 2006), Genzel et al. (2006; RG 2006), Genzel et al. (2008; RG 2008), and Stark et al. (2008; DPS 2008). All data shown here are *uncorrected* for inclination effects. The dashed line denotes  $(\log(\sigma_{\text{mean}}))$  of our sample (note that most galaxies fall below this line), the dotted line represents a simple least-squares fit to the data  $(\log(v_{\text{shear}}/\text{km s}^{-1}) = 0.30 \times \log(M_*/M_\odot) - 1.39)$ . The histogram in the lower part of the plot (arbitrary scale) represents the relative number of galaxies in each logarithmic mass bin for the full sample of 818 optically selected galaxies with stellar mass information in the redshift range  $1.8 < z < 2.6$ . Uncertainties in  $v_{\text{shear}}$  are given where available, the solid line in the lower left corner of the plot indicates the typical uncertainty in  $M_*$ .

evolve into a variety of galaxy types by the present day, including typical  $L^*$  galaxies. Local galaxies with similar star formation properties, however, tend to be gas-rich mergers with multiple nuclei and tidal features (e.g., Sanders et al. 1988; Bushouse et al. 2002), such as the ULIRGS Mrk 273 and IRAS 15250+3609. Similar to the high-redshift sample, these galaxies show large velocity dispersions with little resolved kinematic substructure in the regions of brightest  $H\alpha$  emission, despite relatively strong ( $\sim 200$  km s $^{-1}$ ) and highly disturbed features in lower surface brightness regions (Colina et al. 2005). Perhaps the best analog of these high-redshift galaxies that has been found to date however is the supercompact subsample of UV-luminous galaxies (ScUVLGs) discovered using *Galaxy Evolution Explorer* (GALEX; Heckman et al. 2005). These systems have a similar range of specific SFRs, metallicities, and dust content to high-redshift Lyman break galaxies (see discussion by Heckman et al. 2005; Hoopes et al. 2007; Basu-Zych et al. 2007), and recent evidence (Basu-Zych et al. 2009) indicates that their kinematics are also similar to those of  $z \sim 2$ –3 galaxies with high  $\sigma_{\text{mean}} \gtrsim 80$  km s $^{-1}$  and  $v_{\text{shear}}/\sigma_{\text{mean}} \lesssim 1$ . Many of these ScUVLGs show tidal features and other indications of active mergers on small physical scales and at low surface brightnesses which would not be detectable at high redshift, leading Overzier et al. (2008) to conclude that rapidly star-forming galaxies such as our rest-UV-selected sample are mergers of gas-rich galaxies which have triggered super starbursts on scales of  $\sim 100$ –300 pc.

Numerous morphological studies (e.g., Conselice et al. 2003, and references therein) have interpreted the irregular morpholo-

<sup>16</sup> Where available, we have used stellar masses for the SINS galaxies calculated by Genzel et al. (2008). Otherwise, masses are drawn from our own stellar population modeling. Both estimates are consistent and adopt a Chabrier (2003) IMF. For our galaxies with more than one component we focus on the velocity structure of the most massive component.

**Table 6**  
Other Galaxy Samples

Galaxy	$z^a$	$K_s^b$	$v_{\text{shear}}^c$ (km s <sup>-1</sup> )	$\Delta v_{(\text{ISM}-\text{neb})}^d$ (km s <sup>-1</sup> )	$M_*^e$ (10 <sup>10</sup> M <sub>⊙</sub> )	$\mu^f$	12+ log(O/H) <sup>g</sup>
Förster Schreiber et al. (2006)							
Q1623-BX376	2.4087	20.84	30	-62	0.5	0.81	8.43 ± 0.17
Q1623-BX455	2.4071	21.56	55	-9	0.8	0.87	8.41 ± 0.12
Q1623-BX502	2.1555	22.04	50	-48	0.3	0.92	≲ 8.16
Q1623-BX528	2.2684	19.75	65	-220	12.2	0.18	8.62 ± 0.04
Q1623-BX599	2.3313	19.93	50	-117	6.7	0.37	8.55 ± 0.08
SSA22a-MD41	2.1710	20.5	140	189	2.7 <sup>h</sup>	0.43 <sup>h</sup>	8.43 ± 0.08
Q2343-BX389	2.1728	20.18	235	-76	7.0 <sup>h</sup>	0.22 <sup>h</sup>	8.54 ± 0.08
Q2343-BX610	2.2102	19.21	165	-112	17 <sup>h</sup>	0.15 <sup>h</sup>	8.68 ± 0.01
Q2346-BX404	2.0298	20.05	20	-277	40	0.31	8.50 ± 0.07
Q2346-BX405	2.0308	20.27	30	-79	1.6	0.56	≲ 8.16
Q2346-BX416	2.2406	20.30	70	37	2.5	0.52	8.46 ± 0.07
Q2346-BX482	2.2569	...	100	-175	6.6 <sup>h</sup>	0.31 <sup>h</sup>	8.49 ± 0.07
Genzel et al. (2006)							
BzK15504	2.3834	19.2	171	...	7.7	0.36 <sup>i</sup>	...
Genzel et al. (2008)							
SSA22a-MD41	2.172	20.5	165	189	2.7	0.43 <sup>h</sup>	8.27 ± 0.06
Q2343-BX389	2.174	20.18	261	-76	7	0.22 <sup>h</sup>	8.51 ± 0.04
Q2343-BX610	2.211	19.21	158	-112	17	0.15 <sup>h</sup>	8.66 ± 0.02
Q2346-BX482	2.258	...	213	-175	6.6	0.31 <sup>h</sup>	8.35 ± 0.06
BzK6004	2.387	18.9	146	...	58	0.05 <sup>h</sup>	8.69 ± 0.02
Stark et al. (2008)							
J2135-0102	3.07	...	55	...	0.6	...	8.6

**Notes.**

<sup>a</sup> Systemic redshift, values drawn from the indicated references.

<sup>b</sup> Vega magnitude, uncorrected for line emission. Values based on our own observations except for BzK15504, BzK6004, and SSA22a-MD41.

<sup>c</sup> Values based on indicated references:  $v_r$  from Förster Schreiber et al. (2006),  $v_c \sin i$  from Genzel et al. (2006) and Stark et al. (2008), and  $v_d \sin i$  from Genzel et al. (2008).

<sup>d</sup> Kinematic offset between ISM absorption line redshift and nebular emission-line redshift, calculated from our rest-UV spectra.

<sup>e</sup> Stellar masses for Förster Schreiber et al. (2006) galaxies from our broadband photometry (except where indicated), for all other samples drawn from the indicated reference.

<sup>f</sup> Combines tabulated  $M_*$  with  $M_{\text{gas}}$  from D. K. Erb (2009, private communication) except where indicated.

<sup>g</sup> Oxygen abundance drawn from the indicated reference.

<sup>h</sup> Values from Genzel et al. (2008).

<sup>i</sup> Values from Genzel et al. (2006).

gies of  $z \sim 2$  galaxies as evidence for galaxy–galaxy mergers in the high-redshift universe, and our own kinematic data may further bolster this interpretation in some cases (e.g., HDF-BX1564, Q1700-BX490). One natural suggestion therefore is that the observed multiple-clump morphologies and unusual kinematics of these galaxies may be a consequence of merger activity which prevents the formation of a stable disk at early times (e.g., Ostriker 1990). Such lumps can disrupt the preferred kinematic axis of disk galaxies in the local universe (e.g., Benson et al. 2004), and their effects would likely be stronger at higher redshifts when dark matter haloes were merging more rapidly (e.g., Zentner & Bullock 2003; Fakhouri & Ma 2008). By inflating the velocity dispersion of putative disks in all directions (and not simply perpendicular to the disk), such mergers with either luminous or dark satellites may help mask weak rotational signatures while more massive galaxies with correspondingly larger rotational velocities may naturally be more resilient to such disruption.

However, comparison with cosmological merger trees suggests (Conroy et al. 2008; Genel et al. 2008) that major mergers are too rare to account for the high space density of all  $z \sim 2$  star-forming galaxies. In addition, some of our best merger can-

didates are simultaneously those with the clearest rotation curves (Q1700-BX490). It is therefore unlikely that the uniformly high velocity dispersion of *every single star-forming galaxy* observed to date at redshift  $z \sim 2$  is due to large-scale merger activity, suggesting that the star formation may instead be due to a different triggering mechanism than observed in the local universe.

#### 5.4. An Evolving Picture of Galaxy Formation

According to classic theories of galaxy formation (e.g., White & Rees 1978; Mo et al. 1998; see also the comprehensive review by Baugh 2006), hot-mode spherical accretion dominates the gas accretion history of galaxies. Once a sufficiently massive dark matter halo has virialized, gas collapses through the virial radius of the potential well, heating via shocks to the virial temperature of the host halo. As this gas cools over time (largely by collisionally excited line radiation for haloes with  $10^4 \text{ K} < T < 10^6 \text{ K}$ , and bremsstrahlung radiation for haloes with  $T \sim 10^7 \text{ K}$ ; White 1994) it collapses to form a rotating disk supported by angular momentum which the cooled gas has been unable to shed. This gaseous disk gradually grows over time as gas at progressively greater radii is able to cool and

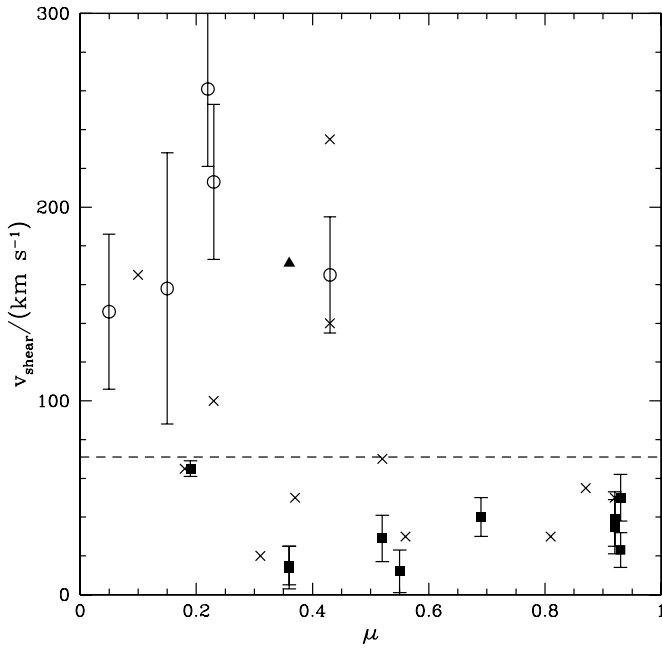


**Figure 11.** Plot of maximum line-of-sight velocity shear vs. gas fraction  $\mu$ . Symbols are the same as in Figure 10, the dashed line denotes  $(\log(\sigma_{\text{mean}}))$  of our sample.

collapse, and is posited to be the home of the bulk of active star formation.

The rotationally supported gas disks predicted by such a classical model are clearly at odds with the randomly directed kinematics observed in a substantial fraction of galaxies at  $z \sim 2$ , prompting us to revisit our understanding of the complex role of gas accretion in galaxy formation. Unlike most galaxies in the local universe, the star-forming galaxies at  $z \sim 2$  contain extremely large quantities of gas as compared to their stellar mass, with the most extreme examples inferred to have gas masses greater than 10 times larger than  $M_*$  (Erb et al. 2006c), and comparable to their kinematically derived dynamical mass. Among the UV-selected galaxies in the  $H\alpha$  sample of Erb et al. (2006c), the inferred gas fraction  $\mu$  (Section 3.2) decreases with increasing  $M_*$ ; Figure 11 recasts the trend of shear velocity in terms of  $\mu$ . Galaxies with the highest gas fraction  $\mu \gtrsim 0.5$  tend to have negligible evidence for rotating kinematic structure and are dominated by randomly oriented velocity dispersions, while those with the lowest gas fractions  $\mu \lesssim 0.5$  have a more obvious preferred axis for their angular momentum with shear velocities  $v_{\text{shear}} \gtrsim 100 \text{ km s}^{-1}$ . We note, however, that while we reproduce the stellar mass–metallicity relation of Erb et al. (2006a; Figure 12, left-hand panel) there is no clear relationship between oxygen abundance and apparent rotational velocity (Figure 12, right-hand panel).

Given that these galaxies have obviously amassed large quantities of cold gas within a very small volume (typically  $r \lesssim 1\text{--}2 \text{ kpc}$ ), the angular momentum of this gas must necessarily be small. There must exist, therefore, some mechanism that can funnel gas to small regions within typical  $z \sim 2$  star-forming galaxies efficiently.

Assuming for a moment that a gaseous disk is the first baryonic structure to form in these halos, gravitational instabilities (e.g., Ostriker & Peebles 1973) within this gas-dominated disk may suffice to produce such concentrated gas reservoirs. Indeed, Noguchi (1999) showed that efficient cooling mechanisms could lead to the fragmentation of gas-dominated disks

into self-gravitating clouds with mass  $\sim 10^9 M_\odot$ , the distribution and relative surface brightness of which might naturally give rise to an irregular, multiple-component morphology similar to those observed for typical star-forming galaxies at  $z \sim 2$  (e.g., Abraham et al. 1996; Conselice et al. 2005; Elmegreen et al. 2005; Lotz et al. 2006; Law et al. 2007b). Likewise, simulations by Bournaud et al. (2007) also suggest that “clump-cluster” galaxies (i.e., those with multiple-component morphologies) are consistent with resulting from the fragmentation of unstable primordial disks. These simulated clumps typically have gas fractions ( $\sim 50\%$ ), SFRs ( $\sim 30 M_\odot \text{ yr}^{-1}$ ), and lifetimes ( $\sim 400 \text{ Myr}$ ) comparable to those of the  $z \sim 2\text{--}3$  star-forming galaxy population (Erb et al. 2006c).

In gas-rich galaxies such as those of our target sample, these massive gaseous clumps may actually drive the dynamical evolution of the entire baryonic component. As discussed by Bournaud et al. (2007), simulated galaxies during the “clump-cluster” phase are highly disturbed with large local velocity dispersions  $\sim 50\text{--}80 \text{ km s}^{-1}$  (i.e., similar to those observed in our target galaxies) and negligible coherent rotational signatures on scales of  $\sim 2\text{--}3 \text{ kpc}$ . At later times ( $\sim 0.5\text{--}1 \text{ Gyr}$ ) these clumps are expected to gradually disperse and sink to the center of the galaxy through dynamical friction, providing a possible mechanism for bulge formation aided by the massive starburst (SFR  $\sim 100 M_\odot \text{ yr}^{-1}$ ) predicted to occur when the remaining clouds merge in the galactic center (e.g., Immeli et al. 2004a, 2004b; Elmegreen et al. 2008). At such late times it is likely that a significant stellar population has been formed which can help stabilize the system against further instability and permit the observation of more regular kinematic structures (as suggested by Figure 10).

Another possibility however is that the classical gas-disk phase may be bypassed entirely by cold flows of low angular momentum gas accreted directly from cosmological filaments (e.g., Kereš et al. 2005; Dekel & Birnboim 2006; Birnboim et al. 2007). Such flows could be responsible for rapidly delivering large quantities of cold gas to the galaxy’s central regions, producing physical conditions that in the local universe are achieved only in gas-rich mergers. The detailed physical structure which might result from such an accretion model is unclear however, especially given the limited ability of numerical models to resolve the relevant spatial scales.

Regardless of the mechanism by which this low angular momentum cold gas is acquired, our observational data suggest the possibility that many young  $z \sim 2$  star-forming galaxies could form roughly spherical early stellar populations in a rapidly accreted pool of low angular momentum gas experiencing a rapidly changing gravitational potential dominated by cooling gas. As the gas fraction of these galaxies decreases this early stellar population may help stabilize an extended gaseous disk which forms at later times from the gradual, more adiabatic accretion of gas from the galactic halo with increasingly greater angular momentum. The dynamics of more massive, evolved galaxies might therefore tend, as we observe, to show greater rotational structure with the formation of such an extended gaseous disk.

Such an interpretation may be bolstered by the observation of a correlation between  $v_{\text{shear}}$  and the kinematics of interstellar absorption lines traced by rest-UV spectroscopy (C. C. Steidel et al. 2009, in preparation). In Figure 13, we plot the offset  $\Delta v_{(\text{ISM} - \text{neb})}$  between the absorption and systemic redshifts as a function of  $v_{\text{shear}}$  for our galaxy sample and that of Förster Schreiber et al. (2006) for which we have rest-UV spectra. While the majority of  $z \sim 2$  galaxies have rest-UV absorption features

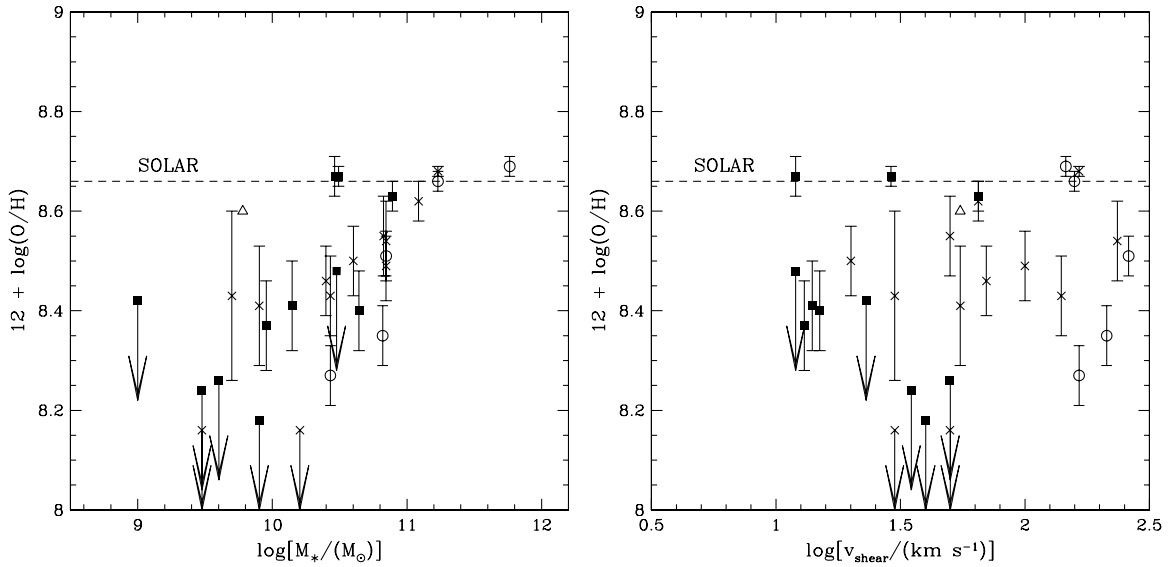


**Figure 12.** Left-hand panel: relationship between stellar mass and metallicity as traced by the oxygen abundance using the  $N2$  calibration of Pettini & Pagel (2004). Right-hand panel: relationship between shear velocity and metallicity. Symbols are the same as in Figure 10, the dashed line indicates solar metallicity (Asplund et al. 2004). Upper limits to the metallicity of galaxies undetected in  $[N II]$  are indicated by the arrows.

with centroids blueshifted relative to the systemic velocity by  $\sim 200 \text{ km s}^{-1}$  (e.g., Pettini et al. 2002; Shapley et al. 2003; C. C. Steidel et al. 2009, in preparation), there is a tendency for galaxies with the greatest observed velocity shear to have lower  $\Delta v_{(ISM-neb)}$ , indicating increased optical depth to UV photons at low systemic velocities (as noted previously by Erb et al. 2006a and Law et al. 2007a). Although the properties of the outflowing gas traced by interstellar absorption lines are generally unrelated to the kinematics of the nebular emission lines (as any nebular emission within the outflowing gas is too low surface brightness to be detectable) it is possible that galaxies with a more well defined kinematic axis could contain a greater fraction of their ISM at close to the systemic redshift (see discussion by C. C. Steidel et al. 2009, in preparation).

This relationship between gas content and  $v_{shear}$  may begin to break down however at lower redshift. Observations by Wright et al. (2009) at  $z \sim 1.6$  find that some galaxies in a similar range of stellar masses and gas fractions to our own sample (and selected in a similar manner) exhibit significant kinematic gradients greater than their apparent velocity dispersion. The applicability of this relation at different redshifts and halo masses is therefore uncertain, but might naturally be expected to evolve along with changes in the cooling time of gas in galactic haloes.

## 6. SUMMARY

We have presented Keck-LGSAO observations of 13 star-forming galaxies at redshift  $z \sim 2-3$  which are representative of the typical stellar mass of the optically selected galaxy sample that dominates the global star formation activity at these epochs. This population of galaxies has a gas-phase velocity dispersion  $\sigma \sim 70 \text{ km s}^{-1}$  that cannot be explained by beam-smearing effects and is an intrinsic property of the gas. These random motions are larger than the amplitude of any systemic velocity shear  $v_{shear}$  within the central 2–3 kpc, although in some cases  $v_{shear}$  may increase if the observed velocity gradient persists to larger radii and fainter surface brightness.

The dominance of random motions (or the absence of significant shear velocity) appears to be related to the stellar mass and

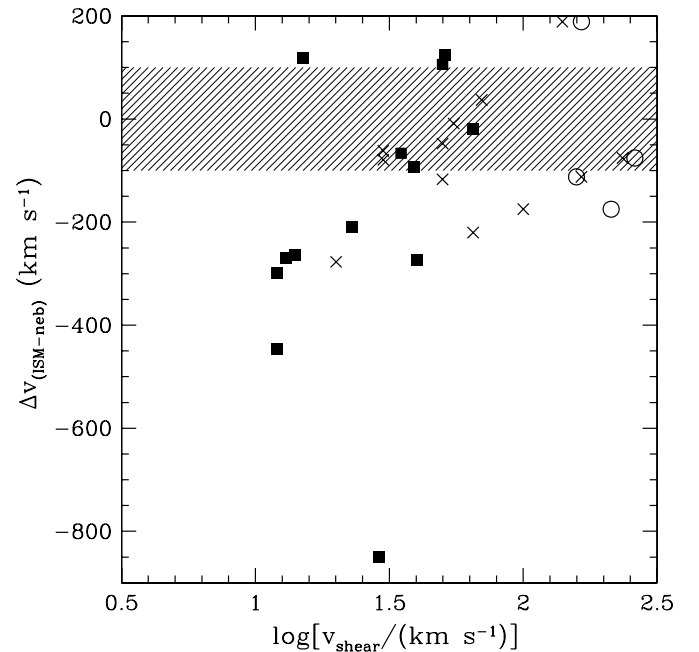


**Figure 13.** Centroid of ISM absorption lines relative to the systemic redshift as a function of  $v_{shear}$ , symbols are the same as in Figure 10. The hatched region denotes a range within  $100 \text{ km s}^{-1}$  of the systemic redshift (roughly the uncertainty of individual values of  $\Delta v_{(ISM-neb)}$ ).

inferred gas fraction: galaxies with larger velocity gradients tend to have larger stellar masses (2–20 times larger than the mean for the parent sample), with smaller values of the gas fraction ( $\mu < 0.5$ ). While there is no similar relation between metallicity and kinematics, there is some evidence to suggest that galaxies with the greatest large-scale velocity structure may contain a greater fraction of their total interstellar medium close to the systemic redshift.

Although the observed kinematics of the high redshift galaxies are similar to those of merger-driven starburst galaxies in the local universe, it is unlikely that mergers are the primary reason for the observed dispersion-dominated kinematics at  $z \sim 2-3$ .



Instead, more efficient cooling and settling of larger amounts of low angular momentum gas (whether attributed to “cold accretion” or some other process) may generically give high-redshift galaxies properties that are produced only in mergers in the local universe. As the large, centrally concentrated gas supply is rapidly converted into stars, the growing stellar population may help stabilize the galaxy and permit the formation of stable disklike structures from higher angular momentum gas accreted over longer timescales.

While such a qualitative picture remains speculative given the current state of both observations and theory, it is without doubt an oversimplification to classify high-redshift galaxies as either “disks” or “mergers”; in fact, many, and possibly even most, are neither. High gas-phase velocity dispersions (and small velocity gradients) are evidently a natural consequence of the instabilities resulting when cold gas becomes dynamically dominant, as it seems to be in the central few kpc of a large fraction of star-forming galaxies at  $z \sim 2-3$ . Learning more precisely how and why this occurs may be the key to understanding galaxy formation.

The authors thank Randy Campbell, Al Conrad, and Jim Lyke for their invaluable assistance obtaining the observations presented herein. D.R.L. also thanks Andrew Benson and Mark Swinbank for constructive discussions, Naveen Reddy for providing stellar mass function data, and the anonymous referee for helpful suggestions which improved the final draft of this manuscript. D.R.L. and C.C.S. have been supported by grants AST-0606912 and AST-0307263 from the US National Science Foundation. Additional support for this work was provided by NASA through Hubble Fellowship grant HF-01221.01 awarded by the Space Telescope Science Institute, which is operated by the Association of Universities for Research in Astronomy, Inc., for NASA, under contract NAS 5-26555. Finally, we wish to extend thanks to those of Hawaiian ancestry on whose sacred mountain we are privileged to be guests.

## APPENDIX

### QUANTIFYING THE MEAN PROPERTIES OF INCLINED SYSTEMS

In cases for which there is obvious morphological or kinematic symmetry indicative of an inclined system, foreshortening of the respective contours may be used to correct apparent rotational velocities for the inclination with confidence. In other cases, however, the degree of such foreshortening may not be obvious, and it is frequently popular to apply an “average” inclination correction to determine the intrinsic rotational velocity in a statistical sense. Confusingly, the value of this average correction frequently differs in the literature, with some authors quoting  $\langle i \rangle = 45^\circ$  and  $\langle \sin i \rangle = \frac{2}{\pi} = 0.64$  (e.g., Erb et al. 2006c; Bouché et al. 2007) and others adopting  $\langle i \rangle = 57.3^\circ$  and  $\langle \sin i \rangle = \frac{\pi}{4} = 0.79$  (e.g., Rix et al. 1997; Weiner et al. 2006). In an effort to foster consistency we present a simple derivation of the correct factor instead of simply stating an adopted value.

The easiest way of visualizing the problem is to imagine the range of possible inclinations  $i$  at which a disk can be viewed. While  $i$  ranges from  $0^\circ$  to  $90^\circ$ , the average value of  $i$  is not  $45^\circ$ , since there are many more ways in which a disk may be viewed from its edge than from its pole. Explicitly, we frame the problem as follows. Given a collection of disks oriented isotropically in space, we wish to determine the mean expected inclination  $i$  between our line of sight to a given disk and the vector normal

to the disk (where  $i = 0^\circ$  represents a disk viewed face-on). It is simplest to reduce this problem to the case of a single disk and consider it from the reference frame of the disk itself. Assuming that a viewing location is chosen at random, the distribution of possible lines of sight will uniformly cover the sky as seen from the reference frame of the disk. The probability  $dP$  that a viewer is located within a given patch of sky is therefore proportional to the differential solid angle  $d\Omega$  subtended by that patch of sky. Adopting a spherical polar coordinate system  $\theta, \phi$  centered on the disk where  $\phi$  is the azimuthal angle and  $\theta$  (ranging from  $-\frac{\pi}{2}$  to  $\frac{\pi}{2}$ ) is the polar angle the differential solid angle is given by

$$d\Omega = \cos \theta d\theta d\phi. \quad (\text{A1})$$

It is therefore possible to calculate the expectation value  $\langle i \rangle$  by integrating over the entire sky. Noting the symmetry present in the problem, we may omit the integral over the azimuthal coordinate  $\phi$  and collapse the polar integral to consider only the range  $\theta = 0-\frac{\pi}{2}$ , reducing the differential solid angle to  $d\Omega = \cos \theta d\theta$ . In this range, the inclination is related to the polar angle by  $\theta = \frac{\pi}{2} - i$ . Therefore,

$$\langle i \rangle = \frac{\int_0^{\frac{\pi}{2}} i \cos \theta d\theta}{\int_0^{\frac{\pi}{2}} \cos \theta d\theta}. \quad (\text{A2})$$

Substituting the identities  $\cos \theta = \sin i$  and  $d\theta = -di$ , we obtain

$$\langle i \rangle = \frac{\int_0^{\frac{\pi}{2}} i \sin i di}{\int_0^{\frac{\pi}{2}} \sin i di} = \frac{[\sin i - i \cos i]_0^{\frac{\pi}{2}}}{[-\cos i]_0^{\frac{\pi}{2}}} = 57.3. \quad (\text{A3})$$

Since the observed velocities of an inclined disk are effectively “foreshortened” by a factor  $\sin i$ , it is usually of interest to calculate the mean velocity reduction factor. Similarly to the calculations performed above, we find

$$\langle \sin i \rangle = \frac{\int_0^{\frac{\pi}{2}} \sin i \cos \theta d\theta}{\int_0^{\frac{\pi}{2}} \cos \theta d\theta} = \frac{\int_0^{\frac{\pi}{2}} \sin^2 i di}{\int_0^{\frac{\pi}{2}} \sin i di} = \frac{\pi}{4} = 0.79. \quad (\text{A4})$$

## REFERENCES

- Abraham, R. G., Tanvir, N. R., Santiago, B. X., Ellis, R. S., Glazebrook, K., & van den Bergh, S. 1996, *MNRAS*, **279**, L47  
 Abraham, R. G., van den Bergh, S., & Nair, P. 2003, *ApJ*, **588**, 218  
 Abraham, R. G., et al. 2007, *ApJ*, **669**, 184  
 Adelberger, K. L., Steidel, C. C., Shapley, A. E., Hunt, M. P., Erb, D. K., Reddy, N. A., & Pettini, M. 2004, *ApJ*, **607**, 226  
 Asplund, M., Grevesse, N., Sauval, A. J., Allende Prieto, C., & Kiselman, D. 2004, *A&A*, **417**, 751  
 Bardeen, J. M., Bond, J. R., Kaiser, N., & Szalay, A. S. 1986, *ApJ*, **304**, 15  
 Basu-Zych, A. R., et al. 2007, *ApJS*, **173**, 457  
 Basu-Zych, A. R., et al. 2009, *ApJ*, submitted  
 Baugh, C. M. 2006, *Rep. Prog. Phys.*, **69**, 3101  
 Benson, A. J., Lacey, C. G., Frenk, C. S., Baugh, C. M., & Cole, S. 2004, *MNRAS*, **351**, 1215  
 Birnboim, Y., Dekel, A., & Neistein, E. 2007, *MNRAS*, **380**, 339  
 Bouché, N., et al. 2007, *ApJ*, **671**, 303  
 Bournaud, F., Elmegreen, B. G., & Elmegreen, D. M. 2007, *ApJ*, **670**, 237  
 Bruzual, G., & Charlot, S. 2003, *MNRAS*, **344**, 1000  
 Bushouse, H. A., et al. 2002, *ApJS*, **138**, 1  
 Calzetti, D., Armus, L., Bohlin, R. C., Kinney, A. L., Koornneef, J., & Storchi-Bergmann, T. 2000, *ApJ*, **533**, 682  
 Chabrier, G. 2003, *PASP*, **115**, 763  
 Chapman, S. C., Blain, A. W., Smail, I., & Ivison, R. J. 2005, *ApJ*, **622**, 772  
 Colina, L., Arribas, S., & Monreal Ibero, A. 2005, *ApJ*, **621**, 725

- Conroy, C., Shapley, A. E., Tinker, J. L., Santos, M. R., & Lemson, G. 2008, *ApJ*, **679**, 1192
- Conselice, C. J., Bershad, M. A., Dickinson, M., & Papovich, C. 2003, *AJ*, **126**, 1183
- Conselice, C. J., Blackburne, J. A., & Papovich, C. 2005, *ApJ*, **620**, 564
- Cowie, L. L., & Barger, A. J. 2008, *ApJ*, **686**, 72
- Daddi, E., Cimatti, A., Renzini, A., Fontana, A., Mignoli, M., Pozzetti, L., Tozzi, P., & Zamorani, G. 2004, *ApJ*, **617**, 746
- Dekel, A., & Birnboim, Y. 2006, *MNRAS*, **368**, 2
- Dib, S., Bell, E., & Burkert, A. 2006, *ApJ*, **638**, 797
- Dickinson, M., Papovich, C., Ferguson, H. C., & Budavári, T. 2003, *ApJ*, **587**, 25
- Elmegreen, B. G., Bournaud, F., & Elmegreen, D. M. 2008, *ApJ*, **688**, 67
- Elmegreen, D. M., Elmegreen, B. G., Rubin, D. S., & Schaffer, M. A. 2005, *ApJ*, **631**, 85
- Erb, D. K., Shapley, A. E., Pettini, M., Steidel, C. C., Reddy, N. A., & Adelberger, K. L. 2006a, *ApJ*, **647**, 813
- Erb, D. K., Steidel, C. C., Shapley, A. E., Pettini, M., & Adelberger, K. L. 2004, *ApJ*, **612**, 122
- Erb, D. K., Steidel, C. C., Shapley, A. E., Pettini, M., Reddy, N. A., & Adelberger, K. L. 2006b, *ApJ*, **647**, 128
- Erb, D. K., Steidel, C. C., Shapley, A. E., Pettini, M., Reddy, N. A., & Adelberger, K. L. 2006c, *ApJ*, **646**, 107
- Fakhouri, O., & Ma, C.-P. 2008, *MNRAS*, **386**, 577
- Förster Schreiber, N. M., et al. 2006, *ApJ*, **645**, 1062
- Förster Schreiber, N. M., et al. 2009, arXiv:0903.1872
- Franx, M., et al. 2003, *ApJ*, **587**, L79
- Genel, S., et al. 2008, *ApJ*, **688**, 789
- Genzel, R., et al. 2006, *Nature*, **442**, 786
- Genzel, R., et al. 2008, *ApJ*, **687**, 59
- Giavalisco, M., Steidel, C. C., & Macchetto, F. D. 1996, *ApJ*, **470**, 189
- Heckman, T. M., et al. 2005, *ApJ*, **619**, L35
- Högbom, J. A. 1974, *A&AS*, **15**, 417
- Hoopes, C. G., et al. 2007, *ApJS*, **173**, 441
- Immeli, A., Samland, M., Gerhard, O., & Westera, P. 2004a, *A&A*, **413**, 547
- Immeli, A., Samland, M., Westera, P., & Gerhard, O. 2004b, *ApJ*, **611**, 20
- Kennicutt, R. C., Jr. 1998, *ApJ*, **498**, 541
- Kennicutt, R. C., Tamblyn, P., Jr., & Congdon, C. E. 1994, *ApJ*, **435**, 22
- Kereš, D., Katz, N., Weinberg, D. H., & Davé, R. 2005, *MNRAS*, **363**, 2
- Larkin, J., et al. 2006, *Proc. SPIE*, **6269**, 42
- Law, D. R., Steidel, C. C., & Erb, D. K. 2006, *AJ*, **131**, 70
- Law, D. R., Steidel, C. C., Erb, D. K., Larkin, J. E., Pettini, M., Shapley, A. E., & Wright, S. A. 2007a, *ApJ*, **669**, 929
- Law, D. R., Steidel, C. C., Erb, D. K., Pettini, M., Reddy, N. A., Shapley, A. E., Adelberger, K. L., & Simenc, D. J. 2007b, *ApJ*, **656**, 1
- Lotz, J. M., Madau, P., Giavalisco, M., Primack, J., & Ferguson, H. C. 2006, *ApJ*, **636**, 592
- Lotz, J. M., Primack, J., & Madau, P. 2004, *AJ*, **128**, 163 (LPM04)
- Martin, C. L. 1997, *ApJ*, **491**, 561
- Martin, C. L., Sawicki, M., Dressler, A., & McCarthy, P. 2008, *ApJ*, **679**, 942
- Mo, H. J., Mao, S., & White, S. D. M. 1998, *MNRAS*, **295**, 319
- Nesvadba, N. P. H., Lehnert, M. D., Davies, R. I., Verma, A., & Eisenhauer, F. 2008, *A&A*, **479**, 67
- Nesvadba, N. P. H., et al. 2006, *ApJ*, **650**, 661
- Noguchi, M. 1999, *ApJ*, **514**, 77
- Ostriker, J. P. 1990, *Proc. Edwin Hubble Centennial Symp. 10, Evolution of the Universe of Galaxies*, ed. R. G. Kron (San Francisco, CA: ASP), **25**
- Ostriker, J. P., & Peebles, J. P. E. 1973, *ApJ*, **186**, 467
- Overzier, R. A., et al. 2008, *ApJ*, **677**, 37
- Papovich, C., Dickinson, M., & Ferguson, H. C. 2001, *ApJ*, **559**, 620
- Papovich, C., Dickinson, M., Giavalisco, M., Conselice, C. J., & Ferguson, H. C. 2005, *ApJ*, **631**, 101
- Papovich, C., et al. 2006, *ApJ*, **640**, 92
- Peter, A. H. G., Shapley, A. E., Law, D. R., Steidel, C. C., Erb, D. K., Reddy, N. A., & Pettini, M. 2007, *ApJ*, **668**, 23
- Pettini, M., & Pagel, B. E. J. 2004, *MNRAS*, **348**, L59
- Pettini, M., et al. 2001, *ApJ*, **554**, 981
- Pettini, M., et al. 2002, *ApJ*, **569**, 742
- Reddy, N. A., Erb, D. K., Steidel, C. C., Shapley, A. E., Adelberger, K. L., & Pettini, M. 2005, *ApJ*, **633**, 748
- Reddy, N. A., & Steidel, C. C. 2009, *ApJ*, **692**, 778
- Reddy, N. A., Steidel, C. C., Erb, D. K., Shapley, A. E., & Pettini, M. 2006a, *ApJ*, **653**, 1004
- Reddy, N. A., Steidel, C. C., Fadda, D., Yan, L., Pettini, M., Shapley, A. E., Erb, D. K., & Adelberger, K. L. 2006b, *ApJ*, **644**, 792
- Reddy, N. A., Steidel, C. C., Pettini, M., Adelberger, K. L., Shapley, A. E., Erb, D. K., & Dickinson, M. 2008, *ApJS*, **175**, 48
- Rix, H.-W., Guhathakurta, P., Colless, M., & Ing, K. 1997, *MNRAS*, **285**, 779
- Sanders, D. B., Soifer, B. T., Elias, J. H., Madore, B. F., Matthews, K., Neugebauer, G., & Scoville, N. Z. 1988, *ApJ*, **325**, 74
- Shapiro, K. L., et al. 2008, *ApJ*, **682**, 231
- Shapley, A. E., Coil, A. L., Ma, C.-P., & Bundy, K. 2005a, *ApJ*, **635**, 1006
- Shapley, A. E., Steidel, C. C., Adelberger, K. L., Dickinson, M., Giavalisco, M., & Pettini, M. 2001, *ApJ*, **562**, 95
- Shapley, A. E., Steidel, C. C., Erb, D. K., Reddy, N. A., Adelberger, K. L., Pettini, M., Barmby, P., & Huang, J. 2005b, *ApJ*, **626**, 698
- Shapley, A. E., Steidel, C. C., Pettini, M., & Adelberger, K. L. 2003, *ApJ*, **588**, 65
- Spergel, D. N., et al. 2007, *ApJS*, **170**, 377
- Springel, V., et al. 2005, *Nature*, **435**, 629
- Stark, D. P., Swinbank, A. M., Ellis, R. S., Dye, S., Smail, I. R., & Richard, J. 2008, *Nature*, **455**, 775
- Steidel, C. C., Adelberger, K. L., Shapley, A. E., Pettini, M., Dickinson, M., & Giavalisco, M. 2003, *ApJ*, **592**, 728
- Steidel, C. C., Shapley, A. E., Pettini, M., Adelberger, K. L., Erb, D. K., Reddy, N. A., & Hunt, M. P. 2004, *ApJ*, **604**, 534
- Swinbank, A. M., Bower, R. G., Smith, G. P., Wilman, R. J., Smail, I., Ellis, R. S., Morris, S. L., & Kneib, J.-P. 2007, *MNRAS*, **376**, 479
- van Starckenburg, L., van der Werf, P. P., Franx, M., Labbé, I., Rudnick, G., & Wuyts, S. 2008, *A&A*, **488**, 99
- Verhamme, A., Schaerer, D., Atek, H., & Tapken, C. 2008, *A&A*, **491**, 89
- Weiner, B. J., et al. 2006, *ApJ*, **653**, 1027
- White, S. D. M. 1994, arXiv:astro-ph/9410043
- White, S. D. M., & Rees, M. J. 1978, *MNRAS*, **183**, 341
- Wright, S. A., et al. 2007, *ApJ*, **658**, 78
- Wright, S. A., et al. 2009, arXiv:0810.5599
- Zentner, A. R., & Bullock, J. S. 2003, *ApJ*, **598**, 49